LA-UR-16-27264
Approved for public release; distribution is unlimited.

Title: (U) Estimating the Photonics Budget, Resolution, and Signal Requirements for a Multi-Monochromatic X-ray Imager

Author(s): Tregillis, Ian Lee

Intended for: Report

Issued: 2016-09-22

LA-UR-YY-XXXXX

(U) Estimating the Photonics Budget, Resolution, and Signal Requirements for a Multi-Monochromatic X-ray Imager

I. L. Tregillis
Plasma Theory and Applications, XCP-6
Los Alamos National Laboratory
Los Alamos, NM 87545

September 13, 2016

Abstract

This document examines the performance of a generic flat-mirror multi-monochromatic imager (MMI), with special emphasis on existing instruments at NIF and Omega. We begin by deriving the standard equation for the mean number of photons detected per resolution element. The pinhole energy bandwidth is a contributing factor; this is dominated by the finite size of the source and may be considerable. The most common method for estimating the spatial resolution of such a system (quadrature addition) is, technically, mathematically invalid for this case. However, under the proper circumstances it may produce good estimates compared to a rigorous calculation based on the convolution of point-spread functions. Diffraction is an important contribution to the spatial resolution. Common approximations based on Fraunhofer (far-field) diffraction may be inappropriate and misleading, as the instrument may reside in multiple regimes depending upon its configuration or the energy of interest. It is crucial to identify the correct diffraction regime; Fraunhofer and Fresnel (near-field) diffraction profiles are substantially different, the latter being considerably wider. Finally, we combine the photonics and resolution analyses to derive an expression for the minimum signal level such that the resulting images are not dominated by photon statistics. This analysis is consistent with observed performance of the NIF MMI.

Contents

List of Figures

List of Tables

1 Introduction

This document contains a general analysis of the properties of a multi-monochromatic x-ray imager (MMI) [1, 2, 3, 4, 5] with flat mirrors. Its secondary purpose is to gather all available information relevant to such an analysis for the specific MMI diagnostics described below. Much of this discussion applies to any pinhole imaging system, such as the heavy emphasis on properly identifying the diffraction regime.

Although an MMI instrument is designed to produce an array of pinhole images, each covering a unique energy domain, the discussion throughout this document pertains to any single pinhole image within that array. Section 2 examines the photonics budget of the instrument. Section 3 estimates the spatial and spectral resolution of the instrument based on an examination of several factors, including both Fraunhofer and Fresnel diffraction. The spatial resolution discussion compares the rigorous approach (based on the convolution of point-spread functions) to common and much easier (but inapplicable in this context) approximations based on quadrature addition. In Section 4, we combine the preceding results to derive lower bounds on the detectable signal level, and compare those limits to MMI data collected on NIF shot N121119. Appendix A examines the relationship between a position on the pinhole plane and the corresponding energy at the detector. Appendix B contains the Yorick code used to calculate Fresnel diffraction profiles in Section 3.

Special emphasis is placed on existing MMI diagnostics at the National Ignition Facility ("NIF") and the University of Rochester Laboratory for Laser Energetics ("Omega"). At the time of this writing, the NIF instrument covered approximately 8 - 13 keV [6]; the range of the Omega MMI instruments was originally approximately 4.5 - 6 keV, which is the focus of the present analysis, but with an additional capability to image 3.3 - 5.5 keV. However, this analysis is applicable to any MMI instrument using flat Bragg reflectors.

Acknowledgments: I wish to thank Peter Hakel (XCP-5) and Scott Hsu (P-24) for feedback on this document, as well as Kirk Flippo (P-24), Rahul Shah (P-24) and Steve Batha (P-DO) for several enlightening conversations. I also thank Tom Murphy (P-24) for bringing my attention to his treatment of the relationship between photon statistics and resolution, which proved crucial for unifying this document, and Fred Wysocki (XCP-DO) for obtaining measurements of an as-built Omega MMI system.

2 Photonics Budget

2.1 Total Number of Photons Available to the Detector (I_0)

Let the "signal level" of the x-ray emission from the capsule be

$$S \quad \left[\mathrm{J \cdot eV^{-1} \cdot sr^{-1}}\right]. \tag{2.1}$$

This is the spatially and temporally integrated emission. In general, it will depend upon the time-varying electron temperature, T_e, and electron density, n_e, plus details of the atomic physics. S might be measured with an absolutely calibrated spectroscopic diagnostic, such as the NIF Supersnout-II instrument, which produces calibrated spectra measured in J eV^{-1} sr^{-1}. Estimating or calculating S requires an atomic physics calculation, either directly or through the use of opacity values. Deriving meaningful constraints on S is the subject of Section 4.

If the burn duration in picoseconds is Δb_{ps}, then the mean signal level per second is

$$\frac{S \ \ [\mathrm{J \cdot eV^{-1} \cdot sr^{-1}}]}{\Delta b_{ps} \cdot 10^{-12} \ \ [\mathrm{s \cdot ps^{-1}}]} = 10^{12} \left(\frac{S}{\Delta b_{ps}}\right) \quad \left[\mathrm{J \cdot eV^{-1} \cdot sr^{-1} \cdot s^{-1}}\right]. \tag{2.2}$$

If the total area of the radiating region in μm^2 is $A_{\mu m^2}$, then the *spectral radiance* of the source—i.e., the mean signal level per second per square centimeter of source—is

$$\begin{aligned} R_{eV} &= \frac{10^{12} \left(\frac{S}{\Delta b_{ps}}\right) \ \ [\mathrm{J \cdot eV^{-1} \cdot sr^{-1} \cdot s^{-1}}]}{A_{\mu m^2} \cdot 10^{-8} \ \ [\mathrm{cm^2 \cdot \mu m^{-2}}]} \\ &= 10^{20} \left(\frac{S}{\Delta b_{ps} \cdot A_{\mu m^2}}\right) \quad \left[\mathrm{J \cdot eV^{-1} \cdot sr^{-1} \cdot s^{-1} \cdot cm^{-2}}\right]. \end{aligned} \tag{2.3}$$

(The spectral radiance is equivalent to the *specific intensity*, I_ν, also known as the *brightness* [7]. This is the quantity obtained by solving the radiative transfer equation along a geometrical ray, such as when post-processing a radiation-hydrodynamic numerical simulation to compute the X-ray self-emission. For example, the Yorick [8] DRAT package computes, for an energy corresponding to frequency ν,

$$I_\nu = I_\nu(0)\, e^{-\tau_\nu} + S_\nu \left(1 - e^{-\tau_\nu}\right)$$

where $\mathrm{I}_\nu(0)$ is the background intensity, S_ν is the source function, and τ_ν the optical depth. Similar calculations in the NLTE regime can be found in [9] and [10], and may be conducted using Peter Hakel's FESTR code [11].)

If the bandwidth of the pinhole image (see Section 2.4) in eV is $\Delta\mathrm{E}_{\mathrm{eV}}$, then the effective *radiance* of the source is approximately

$$\begin{aligned} R \approx R_{eV} \cdot \Delta E_{eV} &= 10^{20} \left(\frac{S}{\Delta b_{ps} \cdot A_{\mu m^2}} \right) \left[\mathrm{J} \cdot \mathrm{eV}^{-1} \cdot \mathrm{sr}^{-1} \cdot \mathrm{s}^{-1} \cdot \mathrm{cm}^{-2} \right] \cdot \Delta E_{eV} \ \ [\mathrm{eV}] \\ &= 10^{20} \left(\frac{S \cdot \Delta E_{eV}}{\Delta b_{ps} \cdot A_{\mu m^2}} \right) \quad \left[\mathrm{J} \cdot \mathrm{s}^{-1} \cdot \mathrm{cm}^{-2} \cdot \mathrm{sr}^{-1} \right]. \end{aligned} \tag{2.4}$$

The energy in Joules of a single emitted photon of energy $\delta\mathrm{E}_{\mathrm{keV}}$ keV is

$$E_{ph} = \delta E_{keV} \cdot 1.602 \times 10^{-16} \ \ \left[\mathrm{J} \cdot \mathrm{photon}^{-1} \right].$$

The mean number of photons of this energy, N_{ph}, emitted per second per steradian per square centimeter of emitting area is therefore the radiance divided by the photon energy, or

$$\begin{aligned} N_{ph} = \frac{R}{E_{ph}} &= \frac{10^{20} \left(\frac{S \cdot \Delta E_{eV}}{\Delta b_{ps} \cdot A_{\mu m^2}} \right) \ [\mathrm{J} \cdot \mathrm{s}^{-1} \cdot \mathrm{cm}^{-2} \cdot \mathrm{sr}^{-1}]}{1.602 \times 10^{-16} \delta E_{keV} \ \ [\mathrm{J} \cdot \mathrm{photon}^{-1}]} \\ &= 6.242 \times 10^{35} \left(\frac{S \cdot \Delta E_{eV}}{\Delta b_{ps} \cdot A_{\mu m^2} \cdot \delta E_{keV}} \right) \quad \left[\mathrm{photon} \cdot \mathrm{s}^{-1} \cdot \mathrm{cm}^{-2} \cdot \mathrm{sr}^{-1} \right]. \end{aligned} \tag{2.5}$$

Let the photon collection interval be $\Delta\mathrm{g}_{\mathrm{ps}}$ picoseconds (e.g., this may represent the width of the gating voltage pulse). Then the number of photons emitted per steradian per square centimeter of emitter *that can be received at the detector during the gating period* is given by

$$I_0 = N_{ph} \ \ \left[\mathrm{photon} \cdot \mathrm{s}^{-1} \cdot \mathrm{cm}^{-2} \cdot \mathrm{sr}^{-1} \right] \cdot 10^{-12} \Delta g_{ps} \ \ [\mathrm{s}]$$

and thus

$$I_0 = 6.242 \times 10^{23} \left(\frac{S \cdot \Delta E_{eV} \cdot \Delta g_{ps}}{\Delta b_{ps} \cdot A_{\mu m^2} \cdot \delta E_{keV}} \right) \ \ \left[\mathrm{photon} \cdot \mathrm{sr}^{-1} \cdot \mathrm{cm}^{-2} \right] \tag{2.6}$$

$$= 6.242 \times 10^{15} \left(\frac{S \cdot \Delta E_{eV} \cdot \Delta g_{ps}}{\Delta b_{ps} \cdot A_{\mu m^2} \cdot \delta E_{keV}} \right) \ \ \left[\mathrm{photon} \cdot \mathrm{sr}^{-1} \cdot \mu\mathrm{m}^{-2} \right] \tag{2.7}$$

where I_0 is the total number of photons *available to the detector* emitted into a unit solid angle per unit area of emitter.

Example: Ge "Jet" Feature

Bruce Hammel has estimated the He_α signal level from a Ge-doped symcap implosion at NIF [12] might be $S = 2 \times 10^{-4}$J eV^{-1} sr^{-1}, given 20 ng of Ge-doped CH ablator mixed into a hotspot with $T_e = 3.5$ keV and $n_e = 3 \times 10^{24}$ cm^{-3}. Given a 100 ps burn width ($\Delta b_{ps} = 100$), a 100 eV bandwidth ($\Delta E_{eV} = 100$), a $10\mu m \times 10\mu m$ emitting area ($A_{\mu m^2} = 100$), and a 70 ps gating window ($\Delta g_{ps} = 70$), the total number of available photons in Ge He_α emission ($\delta E_{keV} = 10.2$) is

$$I_0 = 6.242 \times 10^{23} \cdot \left(\frac{2 \times 10^{-4} \cdot 100 \cdot 70}{100 \cdot 100 \cdot 10.2} \right) = 8.6 \times 10^{18} \text{ photon} \cdot \text{sr}^{-1} \cdot \text{cm}^{-2}.$$

(Sean Regan's HSXRS conceptual design review (CDR) presentation estimates $I_0 = 8.4 \times 10^{18}$ photon $\cdot$ $sr^{-1} \cdot cm^{-2}$ [12].)

Example: NIF Shot N121119

NIF shot N121119 (November 19, 2012) gave a total emission in the Ge He_α line [13] of 1.72 J sr^{-1}. From an emission feature width of 0.353 keV (estimated from plots of the absolutely calibrated spectrum [14]), this gives a signal level $S = 4.87$ J keV^{-1} sr^{-1} or $S = 4.87 \times 10^{-3}$ J eV^{-1} sr^{-1}. (A subsequent reanalysis [15] of the capsule emission for shot N121119 yields 0.872 J sr^{-1} over a line width of 0.14 keV. In that case, the signal $S = 6.23$ J keV^{-1} sr^{-1}. Using that measurement as a starting point would therefore increase all subsequent estimates by ≈28%.) In this shot, the Ge dopant was placed in the inner edge of the capsule shell, so the relevant emitting area is likely much larger than the 100 μm^2 used in the previous example (which pertained to a small "jetlike" feature penetrating an imploding capsule core).

Given a 100 ps burn width ($\Delta b_{ps} = 100$), a 100 eV bandwidth ($\Delta E_{eV} = 100$), a roughly estimated emitting area of $100\mu m \times 100\mu m$ ($A_{\mu m^2} = 10^4$), and a 70 ps gating window ($\Delta g_{ps} = 70$), the total number of available photons in Ge He_α emission ($\delta E_{keV} = 10.2$) is

$$I_0 = 6.242 \times 10^{23} \cdot \left(\frac{4.87 \times 10^{-3} \cdot 100 \cdot 70}{100 \cdot 10^4 \cdot 10.2} \right) \approx 2.1 \times 10^{18} \text{ photon} \cdot \text{sr}^{-1} \cdot \text{cm}^{-2}.$$

2.2 Detected Photons (N_d)

An estimate for the number of photons detected *per resolution element*, N_d, is

$$N_d = I_0 \cdot \Omega_{ph} \cdot A_{res} \cdot \eta \tag{2.8}$$

where I_0 is the total number of photons available to the detector, Ω_{ph} is the solid angle subtended by the pinhole as seen from the source, A_{res} is the area of a resolution element *at the source*, and η is the aggregate detection efficiency of the instrument. This estimate counts discrete photons, although a given instrument is likely to have a raw detection threshold based on a time-integrated flux or a signal level, S, rather than a number of photons. This estimate also disregards noise (however, see Section 4).

(It is important to note that in this discussion "resolution element" is not synonymous with "pixel," as in general these will not be equivalent. The size of an independently resolvable image element is an inherent property of the imaging system, as shown below, and unrelated to the size of detector elements. A monochromatic point source will be blurred into the size and shape of the instrument's resolution element for that energy, which may be larger or smaller than the detector elements.)

In the limit of infinitesimal solid angle and area, the product $\Omega_{ph}A_{res}$ is the étendue of the imager. (Étendue is also known as the "acceptance" or "throughput" of the system.) This quantity is related to Lagrange and optical invariants of the system. It never decreases as light propagates through an imaging system, and is conserved at perfect refractions and reflections [16]. Thus in what follows we are free to disregard reflections from the Bragg mirror while considering ray paths, with the understanding that the resulting expressions for N_d may constitute a lower bound.

The solid angle of the pinhole is easily calculated from the fraction of the total sphere (4π steradians):

$$\frac{\Omega_{ph}}{4\pi} = \frac{A_{ph}}{4\pi L_{tp}^2} \implies \Omega_{ph} = \frac{A_{ph}}{L_{tp}^2} \quad [\text{sr}] \tag{2.9}$$

where A_{ph} is the area of the pinhole aperture, $\pi\,(D/2)^2$, D being the pinhole diameter, and L_{tp} is the distance from TCC (target chamber center) to the pinhole plane.

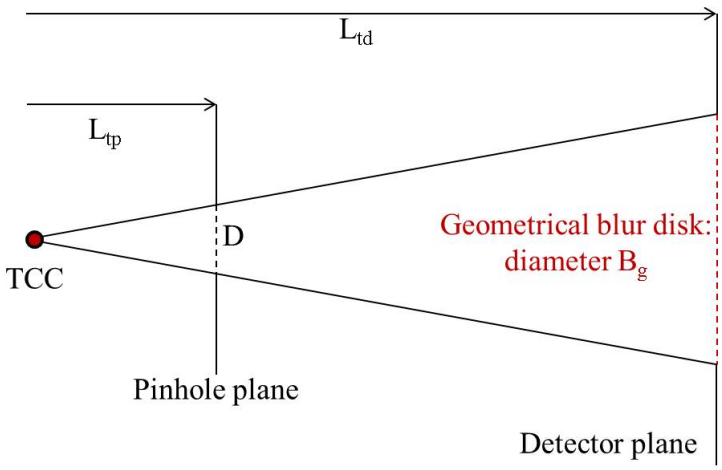

Figure 1: Geometrical blur. Reflection at the Bragg mirror can be disregarded owing to properties of the étendue.

A resolution element *on the detector plane* is the region on the detector over which a monochromatic point source will be smeared. Here we define the geometrical blur region as the disk defined by the magnification of a single point source through the aperture pinhole, as shown in Figure 1. (The edges of the blur disk define the shadow of the aperture in geometrical optics.) The diameter of the geometrical blur region on the detector, B_g, is determined by the relation

$$\frac{(B_g/2)}{L_{td}} = \frac{(D/2)}{L_{tp}} \implies B_g = D\left(\frac{L_{td}}{L_{tp}}\right) = D\,(1+M) \tag{2.10}$$

where L_{td} is the distance from TCC to the detector plane, and M is the instrument magnification, $(L_{td} - L_{tp})/L_{tp}$. Thus the area of the geometrical blur region *on the detector* is

$$A_{blur} = \pi\left(\frac{B_g}{2}\right)^2 = \left(\frac{\pi}{4}\right) D^2\,(1+M)^2\,. \tag{2.11}$$

(This estimate ignores diffraction, which may be non-negligible (see Section 3.1.3.2). However, a detailed treatment of A_{blur} is unnecessary for calculating the number of photons detected per unit area, as shown below.)

The area of a resolution element on the detector is M^2 times the area of a resolution element at the source. Therefore the area of a resolution element *at the source*

is

$$A_{res} = \frac{A_{blur}}{M^2} = \left(\frac{\pi}{4}\right) D^2 \frac{(1+M)^2}{M^2} \quad \left[\text{cm}^2 \cdot \text{resolution element}^{-1}\right] \tag{2.12}$$

and thus we obtain the étendue:

$$\Omega_{ph} \cdot A_{res} = \left[\frac{\pi\,(D/2)^2}{L_{tp}^2}\right] \cdot \left[\left(\frac{\pi}{4}\right) D^2 \frac{(1+M)^2}{M^2}\right] = \frac{\pi^2 D^4\,(1+M)^2}{16 L_{tp}^2 M^2} \quad \left[\text{sr} \cdot \text{cm}^2 \cdot \text{res. elt.}^{-1}\right]. \tag{2.13}$$

The number of photons detected *per independent resolution element at the detector* is therefore

$$N_d = I_0 \cdot \Omega_{ph} \cdot A_{res} \cdot \eta = I_0 \cdot \frac{\pi^2 D^4\,(1+M)^2}{16 L_{tp}^2 M^2} \cdot \eta \quad \left[\text{photon} \cdot \text{res. element}^{-1}\right] \tag{2.14}$$

(Note there is a typographical error in the first form of equation (11) in Koch *et al.*, RSI **76**, 073708 (2005). The correct exponent on D for this expression is 4, as obtained via the above derivation, rather than 2, as written in the above reference.)

Again, this is a measure of the number of photons per independent image element, *not* per detector element (i.e., not per pixel). A more common measure is the number of photons detected per unit area of detector, frequently per square micron. To obtain that number, we normalize $\mathrm{N_d}$ by the area of the geometrical blur region *at the detector* in the appropriate units ($\mu\text{m}^2 \cdot \text{res. element}^{-1}$). Doing so yields

$$N_{\mu m^2} = \frac{N_d}{A_{blur}} = \frac{I_0 \cdot \Omega_{ph} \cdot A_{res} \cdot \eta}{A_{blur}} = I_0 \cdot \frac{\Omega_{ph}}{M^2} \cdot \eta = I_0 \cdot \frac{\pi D^2}{4 L_{tp}^2 M^2} \cdot \eta \quad \left[\text{photon} \cdot \mu\text{m}^{-2}\right]. \tag{2.15}$$

Because this estimate is independent of $\mathrm{A_{res}}$ and $\mathrm{A_{blur}}$, it doesn't require a sophisticated model for the blur disk size. Thus diffraction from the pinhole and Bragg reflector is immaterial to this discussion. These effects are analyzed in Section 3.

If the area of a detector pixel is $\mathrm{A_{pix}}$ μm^2, then

$$N_{pix} = N_{\mu m^2} \cdot A_{pix} = I_0 \cdot \frac{\pi D^2 A_{pix}}{4 L_{tp}^2 M^2} \cdot \eta \quad \left[\text{photon} \cdot \text{pixel}^{-1}\right]. \tag{2.16}$$

Example: Ge "Jet" Feature

From above, we have $I_0 = 8.6 \times 10^{10}$ photon sr^{-1} μm^{-2}.

For the NIF MMI, M = 6 and L_{tp} = 16.667 cm = $1.6667 \times 10^5 \mu$m. If the pinhole diameter (D) is 10 μm, then we'd expect the NIF MMI to detect

$$N_{\mu m^2} = 8.6 \times 10^{10} \cdot \frac{\pi 10^2}{4 \cdot (1.6667 \times 10^5)^2 \cdot 6^2} \cdot \eta = 6.75\ \eta \text{ photon} \cdot \mu\text{m}^{-2}.$$

Example: NIF Shot N121119

From above, $I_0 = 2.1 \times 10^{10}$ photon sr^{-1} μm^{-2}.

Again using M = 6, L_{tp} = 16.667 cm, and D = 10 μm, we would expect the NIF MMI to detect

$$N_{\mu m^2} = 2.1 \times 10^{10} \cdot \frac{\pi 10^2}{4 \cdot (1.6667 \times 10^5)^2 \cdot 6^2} \cdot \eta = 1.65\ \eta \text{ photon} \cdot \mu\text{m}^{-2}. \quad (2.17)$$

2.3 Detection Efficiency (η)

The aggregate detection efficiency, η, comprises contributions from three factors:

$$\eta = \eta_{filter} \cdot \eta_{Bragg} \cdot \eta_{MCP}.$$

The first factor, η_{filter}, represents X-ray attenuation owing to propagation through the blast shield and any additional filters. The second factor, η_{Bragg}, accounts for the reflectivity of the Bragg mirror. The final factor, η_{MCP}, is a catch-all that incorporates the overall efficiency of the multichannel plate (MCP) and subsequent electronics. All factors are energy-dependent. (Note that errors in the flat-fielding of the MMI energy response can introduce significant errors in the inferred plasma quantities, such as electron temperature [17].)

2.3.1 Blast Shield and Filters (η_{filter})

It is possible for the target to generate a significant amount of particulate debris. The debris leaves TCC with a range of kinetic energies and sizes; the smallest pieces

may pass through the pinholes. It is therefore possible for particles to enter the MMI and damage the instrument. Thus a blast shield (typically several layers of one or more materials in multiple locations) is installed behind the pinhole array. The blast shield also acts as an X-ray filter, and may produce significant attenuation. For instance, the transmission through 2 mm of Kapton ranges from 18% at 8 keV to 67% at 12.85 keV. The X-ray transmission of the shield can be computing online via the Center for X-ray Optics at Lawrence Berkeley National Laboratory [18].

2.3.2 Reflectivity (η_{Bragg})

MMI instruments use crystals or multilayer materials as low-incidence-angle gratings. While the reflected intensity is a delta function of incidence angle for an ideal grating, imperfections and other real-world effects give rise to nonzero reflected intensities at small variations from the $\mathrm{n} = 1$ Bragg condition. A plot of the reflected intensity at a fixed detector location as a function of incidence angle is known as the rocking curve [19] (see Section 3.1.4).

The Bragg mirrors for the NIF and Omega MMI instruments are multilayer materials comprising approximately 300 periods of alternating W and B_4C layers deposited atop a substrate of crystalline silicon. The average inter-layer spacing of the composite W/B_4C material is $\mathrm{d} = 1.5 \pm 0.0015$ nm with a uniformity of ± 0.007 nm [20].

The performance of the multilayer has been calculated [20] for incident plane waves between 9 and 12.5 keV. For pinhole image energies near the low end of the NIF instrument range, 8 keV, an integrated Bragg reflectivity of 30% is characteristic of the multilayer. For pinhole image energies near the upper end of the intrument range, 13 keV, the average reflectivity is closer to 20%. The Bragg contribution to the NIF MMI photonics budget is therefore weakly dependent upon energy.

No analogous data exist for energies within the domain of the Omega MMI.

2.3.3 Multichannel Plate (η_{MCP})

The efficiency of the multichannel plate (MCP) is determined by several factors including (but not limited to) the gold photocathode response function [21] (which measures the energy-dependent efficiency of producing an electron for the scintillator fibers); the amplification of electrons within the scintillator fibers (which therefore depends upon the gain); and the performance of the phosphor plate. Some of these factors will be strongly energy dependent, such as the photocathode response function. The energy-dependent quantum efficiency of a gold photocathode can be found in [21]. A common energy-independent estimate of the MCP efficiency [12] is 7%, however a superior energy-dependent response function can be found in [22].

Example: Ge "Jet" Feature

At 10.2 keV, the transmission through 2.5 mm (98.43 mils) of Kapton is 37%. The reflectivity of the NIF MMI Bragg mirror at this energy is 30%, and the energy-independent MCP efficiency is roughly 7%. Thus

$$\eta = 0.37 \cdot 0.30 \cdot 0.07 = 7.77 \times 10^{-3}$$

and, using our previous calculation,

$$N_{\mu m^2} = 6.75 \cdot 7.77 \times 10^{-3} \text{ photon} \cdot \mu\text{m}^{-2} = 0.052 \text{ photon} \cdot \mu\text{m}^{-2}$$

Example: NIF Shot N121119

Using the same η value as above, we get

$$N_{\mu m^2} = 1.65 \cdot 7.77 \times 10^{-3} \text{ photon} \cdot \mu\text{m}^{-2} = 0.013 \text{ photon} \cdot \mu\text{m}^{-2}$$

2.4 Monochromaticity of Pinhole Images ($\Delta\mathrm{E_{eV}}$)

The finite sizes of the source and pinhole lead to significant variation in the incidence angles for geometrical rays arriving at the Bragg reflector. Thus, rather than being truly monochromatic, each pinhole image in the MMI array will encompass a range of energies, $\Delta\mathrm{E_{eV}}$. The basic geometry is illustrated by the cartoon in Figure 2.

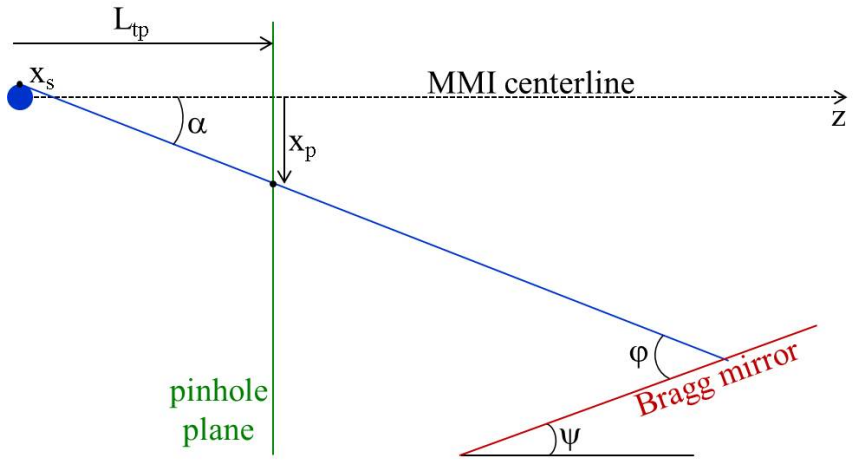

Figure 2: Variation of incidence angles on the Bragg mirror.

A ray from the source to the Bragg mirror makes an angle α with the MMI centerline, which depends on the emission location at the source (x_s) and the location at which the ray intersects the pinhole plane (x_p). The tilt angle of the mirror is ψ, and the Bragg angle for this ray is φ. From the diagram, we see that $\varphi = \alpha + \psi$. Thus the n=1 Bragg condition yields

$$E(\alpha) = \frac{hc}{2d\sin(\alpha+\psi)}; \quad \alpha = \tan^{-1}\left(\frac{x_p - x_s}{L_{tp}}\right) \tag{2.18}$$

and

$$\frac{dE}{d\alpha} = -\frac{hc}{2d}\cot(\alpha+\psi)\csc(\alpha+\psi). \tag{2.19}$$

(While energy variation across the mirror is a strong function of x_p it depends only weakly on y_p, as shown in Appendix A.)

We consider the individual contributions of the pinhole and source sizes separately. In what follows, we consider source sizes of 200, 250, and 300 μm for the NIF MMI (based on empirical observations of DIME shots) and source sizes of 100, 115, and 130 μm for the Omega MMI (these being the core sizes for which the various Omega MMI pinhole designs were intended [23]). We consider NIF pinholes of 10, 35, and 50 μm, and Omega pinholes of 5, 10, and 15 μm. These choices give approximately the same range of source/pinhole size ratios for both instruments (4 - 30 for the NIF MMI, and 6.7 - 26 for the Omega MMI). If the aperture becomes too large

compared to the source, it may be better modeled as a penumbral aperture rather than a pinhole aperture [24, 25].

2.4.1 Point Source, Extended Pinhole

First, consider the case of a point source located at the origin (target chamber center, or TCC) and a pinhole of diameter D centered at x_{ph}. Incidence angles will vary at the mirror as illustrated in Figure 3.

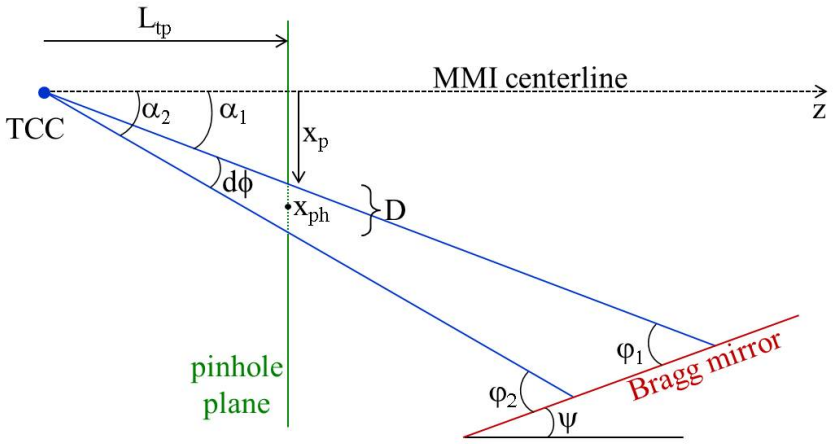

Figure 3: Variation of incidence angles owing to a finite pinhole size.

In this case, we have $x_s = 0$, $x_p = x_{ph} \pm \frac{1}{2}D$, and $\alpha_2 = \alpha_1 + d\phi$. The energy variation across the pinhole is therefore

$$\Delta E_{eV} = |E(\alpha_2) - E(\alpha_1)|$$

Plots of ΔE_{eV} for a reasonable range of x_{ph} values are shown in Figure 4 for the Omega MMI and figure 5 for the NIF MMI. Both instruments use a W/B_4C multilayer with $d \approx 15$Å interlayer spacing.

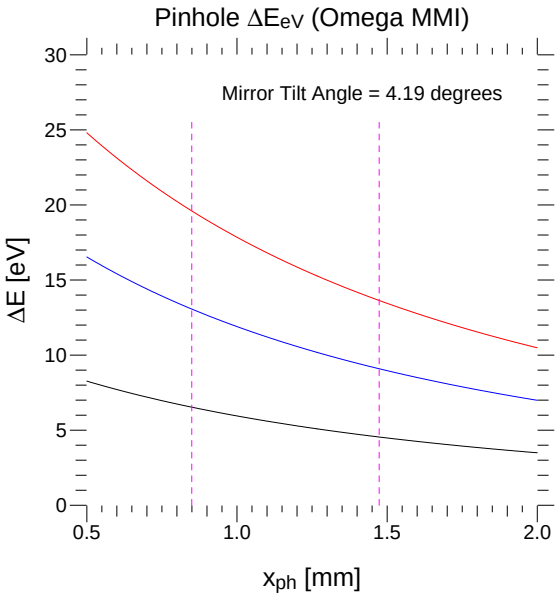

Figure 4: Omega MMI ΔE_{eV} for a point source and extended pinhole, as a function of pinhole location. Pinhole diameters are 5 μm (black), 10 μm (blue), and 15 μm (red).

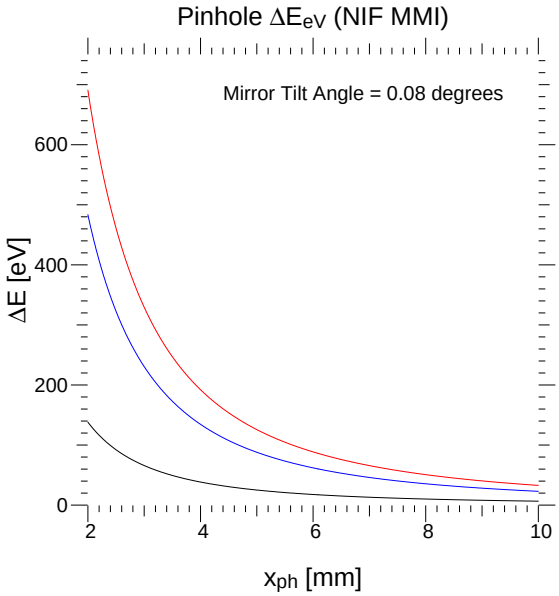

Figure 5: NIF MMI ΔE_{eV} for a point source and extended pinhole, as a function of pinhole location. Pinhole diameters are 10 μm (black), 35 μm (blue), and 50 μm (red).

Pinholes on the Omega MMI instruments are distributed between 0.8495 mm above and 1.4735 mm below the MMI centerline [23]; these values are marked in figure 4. For the Omega MMI, ΔE_{eV} ranges from 5 - 20 eV for 5 - 15 μm pinholes. In contrast, on the NIF MMI, ΔE_{eV} may exceed 100 eV for 10 μm pinholes within 2.4 mm of the NIF MMI centerline, or for 50 μm pinholes within 5.6 mm of the centerline.

These estimates provide a lower bound on the bandwidth of *point source* images, owing strictly by the finite size of the pinhole.

2.4.2 Extended Source, Infinitesimal Pinhole

Now consider the case of an extended source. If the source is sufficiently larger than the pinhole aperture, the pinhole may be treated as an infinitesimal point. This geometry is illustrated in Figure 6.

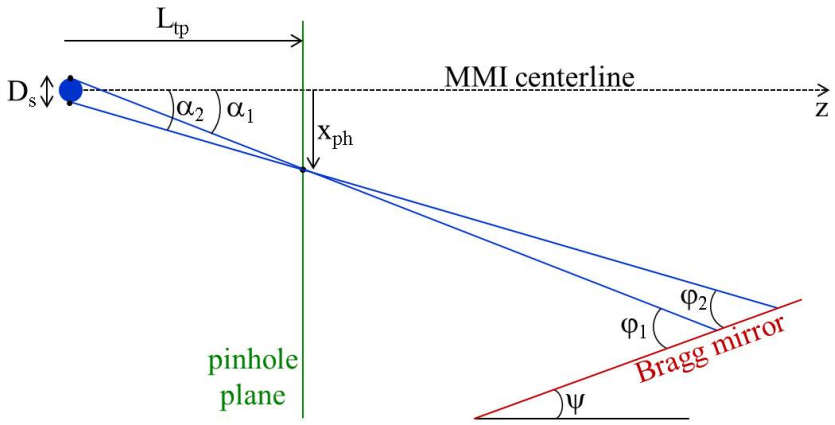

Figure 6: Variation of incidence angles owing to a finite source size.

In this case $x_p = x_{ph}$ and $x_s = \pm 0.5\ D_s$ where D_s is the source diameter. Plots of ΔE_{eV} for a reasonable range of D_s values are shown in Figure 7 for the Omega MMI and Figure 8 for the NIF MMI.

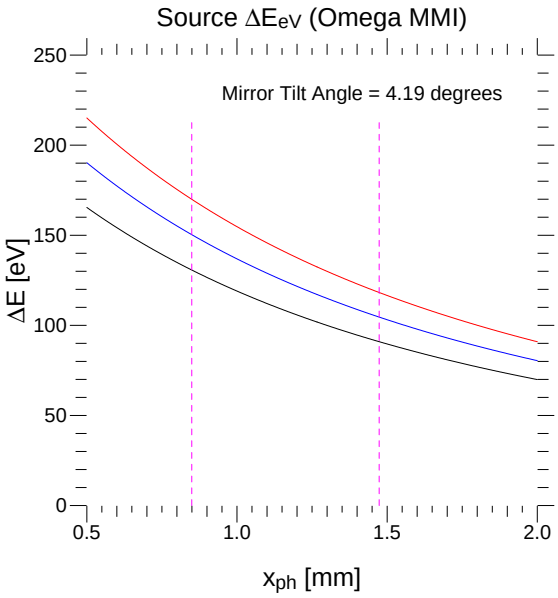

Figure 7: Omega MMI ΔE_{eV} for an extended source and infinitesimal pinhole, as a function of pinhole location. Source sizes are 100 μm (black), 115 μm (blue), and 130 μm (red).

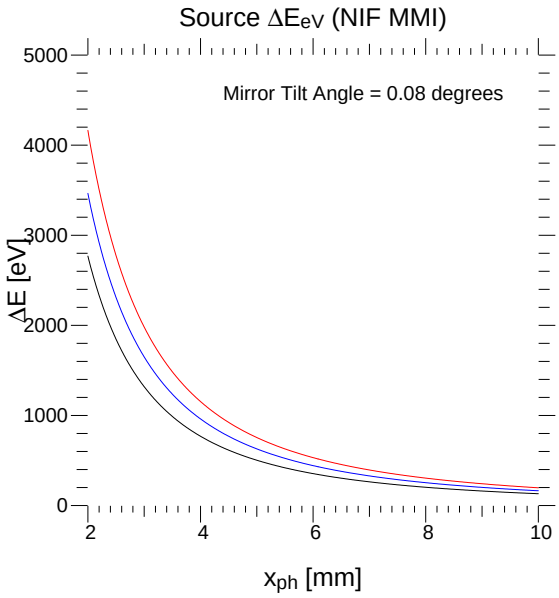

Figure 8: NIF MMI ΔE_{eV} for an extended source and infinitesimal pinhole, as a function of pinhole location. Source sizes are 200 μm (black), 250 μm (blue), and 300 μm (red).

The Omega MMI pinhole designs are intended to accommodate core sizes between 100 and 130 μm [23]; as above, the range of allowed pinhole locations is marked on Figure 7. ΔE_{eV} values for this instrument range from 90 - 170 eV for these core sizes. On the NIF MMI, we see that ΔE_{eV} will exceed 150 eV for pinholes 1 cm from the centerline. The bandwidth grows to several hundred eV at 5 mm.

Comparison of figures 4, 5, 7, and 8 shows the bandwidth contribution from the finite source size is nearly an order of magnitude greater than the contribution from the finite pinhole size. This is to be expected, as the pinhole apertures are required to be negligible compared to the source size (as opposed to penumbral apertures).

3 Spatial and Spectral Resolution

We begin by noting the resolution in the orthogonal directions of a 2D MMI pinhole image may have different contributing factors. Typically the energy variation across the MMI detector plane varies strongly with pinhole position in one direction but only weakly in the orthogonal direction. (See appendix A.) We ignore the variation in the weak direction. This is justified because most MMI analysis procedures implicitly assume the spectral variation is strictly one-dimensional [26, 27]. In what follows, we assume the instrument magnification does not vary across the field, and is the same in the x- and y-directions. In practice it may vary, for instance if the detector and reflector are misaligned. For the purpose of calculating the diffraction contributions we assume all pinhole apertures to be perfectly circular, although in practice fabrication difficulties may produce elliptical pinholes.

The spatial resolution limit is established by the width (not radius) of a monochromatic point-spread function (PSF) image. Throughout this section, we compare two methods for estimating that width. A quadrature addition method is commonly used in the literature [28, 29]. While straightforward, this method relies upon unjustified physical assumptions, and may lead to significant underestimation of the PSF width, depending on the diffraction regime. The correct approach, which involves computing a chain of distinct PSF convolutions, is more computationally intensive. However, we will derive approximations for the diffraction PSF in both the far- and near field which greatly simplify the PSF convolution method and lead to semi-analytic estimates consistent with results derived by rigorous numerical computation.

We conduct all calculations at the detector and convert to a source resolution at the end. These estimates do not account for effects that stem from the finite time gating of the detector at a particular location, and/or the finite interval for the gating pulse to sweep across the photocathode. Such effects may include motion blur within a particular pinhole image, or the translation of temporal variations in the line/continuum ratio into spatial variations across the detector plane.

3.1 Spatial Resolution

3.1.1 Convolution of Point Spread Functions

The final image on the detector plane is the convolution of the source profile with the PSFs of the various instrument elements. In this case the pinhole, the Bragg reflector (i.e., the crystal or multilayer), and the detector each contribute their own PSF to the final image. Additional elements may contribute, but here we restrict our attention to these factors. By denoting the radial image intensity by I(r) and the radial source profile by S(r) (not to be confused with the signal level, S), and the PSFs by P, the fundamental relationship can be written

$$I(r) = \left\{ \left[\left(S\left(r\right) * P_{ph}\left(r\right) \right) * P_{Bragg}\left(r\right) \right] * P_{det}\left(r\right) \right\} \tag{3.1}$$

where "$*$" denotes convolution. Each PSF represents a normalized distribution of intensities or, equivalently, irradiances (power received per unit area). The normalization is important for keeping each convolution operation flux-conservative.

The pinhole PSF, P_{ph}, has two components: a contribution from the geometrical shadow of the aperture (the ray-optics contribution), plus a contribution from diffraction [28, 29]. By applying the associative property of convolutions we obtain the aggregate PSF of the system:

$$P_{system}(r) = P_{geom}\left(r\right) * P_{diff}\left(r\right) * P_{Bragg}\left(r\right) * P_{det}\left(r\right). \tag{3.2}$$

Approximating the spatial resolution limit of the instrument means estimating the width of the system PSF.

3.1.1.1 Special Case: Gaussian PSFs

Consider a case where the source profile and every PSF is Gaussian. Then let us define σ_{S}^2 to be the variance of S(r), σ_{geom}^2 to be the variance of P_{geom}, etc. The convolution of a pair of Gaussians produces another Gaussian, and the resulting variance is simply the sum of the original variances. In this circumstance I(r) will be a Gaussian with variance given by

$$\sigma_I^2 = \sigma_S^2 + \sigma_{geom}^2 + \sigma_{diff}^2 + \sigma_{Bragg}^2 + \sigma_{det}^2 \tag{3.3}$$

When $\sigma_S^2 \to 0$, the extended source becomes a point source, and

$$\Sigma_0^2 \equiv \sigma_{geom}^2 + \sigma_{diff}^2 + \sigma_{Bragg}^2 + \sigma_{det}^2 \tag{3.4}$$

is the variance of the system PSF. If we equate the *radius* of the system PSF with its standard deviation (i.e., the square root of the variance), then $2\,\Sigma_0$ is the spatial resolution limit of the system (the PSF width).

Calculating the quadratic sum is trivial for known Gaussian standard deviations, σ. Thus, the convenience of Equation 3.4 makes it the basis of many resolution estimates in the X-ray pinhole imaging literature [28, 29]. *However, it is only applicable to a chain of Gaussian point spread functions, or to PSFs that can be well-approximated by a Gaussian.* As shown below, the Gaussian assumption fails for P_{diff} in the near-field regime, and it is patently incorrect for P_{geom}.

3.1.1.2 General Case: Non-Gaussian PSFs

In what follows, we will denote the effective width (diameter) of each PSF by D rather than 2σ to emphasize that these functions might be non-Gaussian. An estimate for the resolution limit at the detector, based on the Gaussian case but commonly used in the literature, is [28, 29]

$$\begin{aligned} D_{x,y}^2 =& D_{det}^2 + D_{ph}^2 + D_{Bragg}^2 \\ =& D_{det}^2 + D_{geom}^2 + D_{diff}^2 + D_{Bragg}^2 \end{aligned} \tag{3.5}$$

where D_x and D_y are the axes of the ellipse into which a monochromatic point source is blurred (here assumed to be equal).

3.1.2 Detector (P_{det}, D_{det})

According to George Kyrala [30], the resolution of the MCP used by the NIF MMI on shot N121119 was 50 μm. Kyrala also states [31] the resolutions of the NIF and Omega MCPs are approximately the same (50 μm). (It should be noted that the final *scanned* resolution of the film used for the Omega MMI instruments may be 20 μm or smaller, according to Rahul Shah [32]. However, this is distinct from the resolution of the detector during data collection.)

For simplicity, and lacking more specific information, we assume the detector PSF to be Gaussian. In that case, the standard deviation σ_{det} in Equation 3.4 is 10.62 μm, which yields a Gaussian FWHM = 2.3548σ = 25.0 μm. Alternatively, if we estimated the resolution via Equation 3.5, we would use $\mathrm{D_{det}} = 50\mu$m.

3.1.3 Pinhole ($\mathrm{P_{ph}}$,$\mathrm{D_{ph}}$)

Two factors contribute to the pinhole point-spread function: a geometric component arising from the finite size of the aperture, and a contribution from diffraction through the aperture [28, 29].

3.1.3.1 Geometric Component ($\mathrm{P_{geom}}$, $\mathrm{D_{geom}}$)

The geometrical shadow of the pinhole aperture defines a region of diameter $\mathrm{D_{geom}}$. This is the geometrical blur disk arising from the projection of a point source through a single pinhole, as shown in Figure 1. (Recall that the Bragg mirror can be ignored when examining this property of the system because the étendue, which is related to optical invariants of the system, is conserved in perfect reflections, as described in Section 2.2.) As shown in Equation 2.10, the diameter of the geometrical blur region on the detector is simply $\mathrm{D}(1 + \mathrm{M})$, where D is the pinhole diameter and M is the instrument magnification. Thus

$$D_{geom} = D(1 + M) \tag{3.6}$$

which, based on the design specifications, yields $\mathrm{D_{geom}} \approx 7\mathrm{D}$ for the NIF MMI instrument and $\mathrm{D_{geom}} \approx 9.6\mathrm{D}$ for the Omega MMI instruments. (The empirical magnification of the as-built instruments may vary. Rahul Shah has obtained $M = 7.5$ for the Omega MMI, based on comparison of the known pinhole spacings and the measured image spacings [33].)

$\mathrm{D_{geom}}$ is sufficient to compute the ray-optics contribution to the system resolution limit according to Equation 3.5. But in order to compute the convolutions correctly, as in Equation 3.2, we must also derive a functional form for the PSF, $\mathrm{P_{geom}}$. Consider Figure 1. Let the radiant flux arriving at the center of the detector (i.e., along the central axis) be $\mathrm{F_0}$. Then, by the inverse square law, the radiant flux arriving at the

detector screen a distance r from the central axis must be

$$F(r) = \begin{cases} F_0 \dfrac{L_{td}^2}{L_{td}^2 + r^2} = \dfrac{F_0}{1 + \left(\frac{r}{L_{td}}\right)^2} & |r| < R_{geom} \\ 0 & |r| \geq R_{geom} \end{cases} \tag{3.7}$$

where $R_{geom} = 0.5 D_{geom}$. Note that $R_{geom} \ll L_{td}$ for the system configurations under consideration here. Then $F(r) \approx F_0$ for $|r| < R_{geom}$ and 0 elsewhere, meaning P_{geom} is well approximated by a normalized boxcar function:

$$P_{geom}(r) = \frac{1}{2R_{geom}} \left[\Theta\left(r + R_{geom}\right) - \Theta\left(r - R_{geom}\right) \right] \tag{3.8}$$

where Θ denotes the Heaviside step function. This cannot be approximated by a Gaussian. Because the geometric contribution from the pinhole is *always* a factor in the resolution, the quadrature addition method is *never* mathematically justified, as at least one contributing factor is distinctly non-Gaussian. Nevertheless under certain circumstances it may produce decent estimates, as shown in Section 3.1.6.

3.1.3.2 Diffraction (P_{diff}, D_{diff})

A proper treatment of the diffraction contribution depends on whether the detector lies in the far-field regime, in which case the Fraunhofer approximation applies, or in the near-field regime, in which case a more complicated Fresnel diffraction calculation is required. (Both approximations are derived from scalar diffraction theory.)

The regime is determined by the dimensionless Fresnel number

$$F = \frac{R^2}{\lambda L} = \frac{(D/2)^2}{\lambda L} \tag{3.9}$$

where R is the aperture radius, λ is the wavelength, and L is the distance from the aperture to the detector plane. (On axis, $L = L_{td} - L_{tp}$. We use this approximation for L when estimating F.) The Fraunhofer approximation applies for $F \ll 1$, while the Fresnel approximation applies for $F \gtrsim 1$ [34].

Given $\lambda = hc/E = (12.4 \times 10^{-4}/E_{keV})\,\mu m$, we have $F = 2.02 \times 10^2\ D^2\ E_{keV}/L$ where D and L are measured in μm. As in Section 2.4, we consider 10, 35, and 50 μm NIF MMI pinholes, and 5, 10, and 15 μm pinholes for the Omega MMI.

The Fresnel number for the NIF MMI (L = 1.0 m) is

$$F_{NIF} = 2.02 \times 10^{-4}\ D^2\ E_{keV} \tag{3.10}$$

The energy range for the NIF MMI instrument is approximately 8-13 keV. Thus, it has a Fresnel number $F_{NIF} \approx 0.16 - 0.26$ for 10 μm pinholes, nominally in the Fraunhofer (far field) regime, while for pinholes larger than 25 μm the Fresnel number $F_{NIF} > 1$, firmly in the Fresnel regime.

The Fresnel number for the Omega MMI (L = 27.0 cm) is

$$F_{Omega} = 7.48 \times 10^{-4}\ D^2\ E_{keV} \tag{3.11}$$

The energy range of the Omega MMI instrument is approximately 4.5 - 6.0 keV. Thus $F_{Omega} < 1$ for 5 and 10 μm pinholes. But for 15 μm pinholes, $F_{Omega} \approx 0.76$ for 4.5 keV and $F_{Omega} \approx 1.01$ for 6.0 keV. Thus when D = 15 μm, the diffraction resides in a transitional regime between the far- and near-field approximations. ($F_{Omega} > 1$ for all energies when D = 17.24 μm.)

The Fresnel numbers are plotted in Figures 9 and 10.

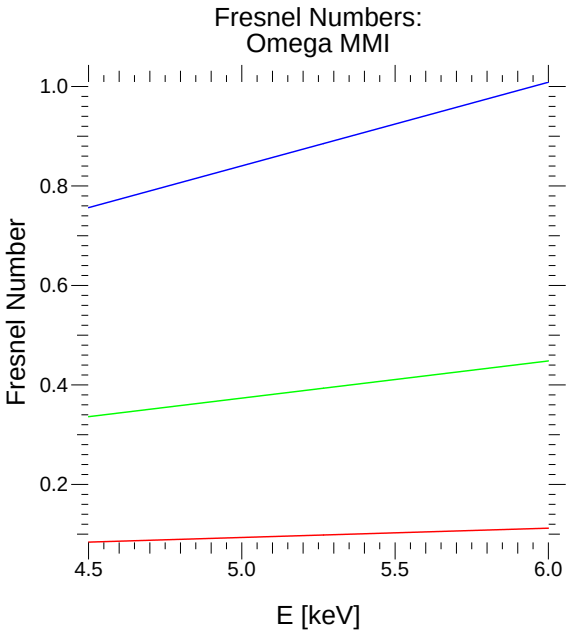

Figure 9: Fresnel numbers for the Omega MMI. Red: 5 μm pinhole; Green: 10 μm pinhole; Blue: 15 μm pinhole.

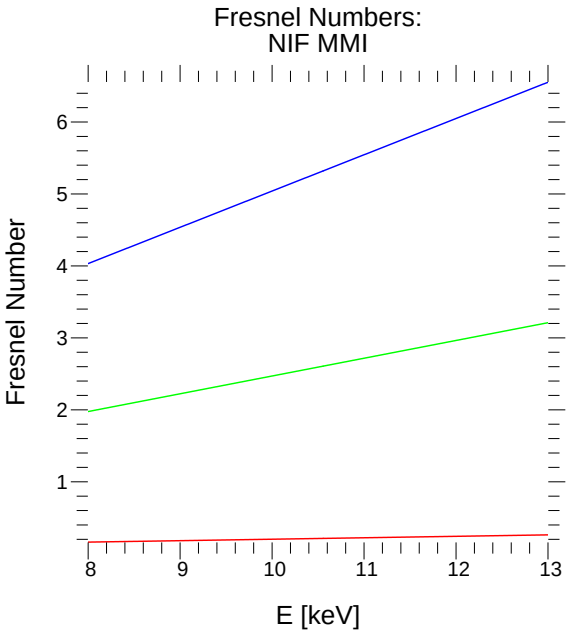

Figure 10: Fresnel numbers for the NIF MMI. Red: 10 μm pinhole; Green: 35 μm pinhole; Blue: 50 μm pinhole.

Fraunhofer (far-field) Diffraction The diffracted spot size for a circular aperture in the Fraunhofer case is set by the angular radius of the Airy disk:

$$\sin\theta \approx \frac{1.22\lambda}{D} \tag{3.12}$$

where the numerical factor $1.22 \approx 3.8317/\pi$ (3.8317 being the first nontrivial zero of the Bessel function J_1). The above relationship is the Rayleigh resolution criterion. Again using $\lambda = (12.4 \times 10^{-4}/\mathrm{E_{keV}})\,\mu$m, we have

$$\sin\theta \approx \frac{1.51 \times 10^{-3}}{D\ E_{keV}} \tag{3.13}$$

where D is measured in microns, as usual. Thus we have $\sin\theta \ll 1$ for all relevant energies and aperture sizes. Then $\sin\theta \approx \theta$ and therefore the linear *diameter* of the Airy disk, as used in the quadrature addition method, is

$$D_{diff} \approx \frac{2.44\lambda L}{D} \equiv D_{Airy}. \tag{3.14}$$

The true far-field diffraction PSF is given by the Airy intensity pattern

$$P_{diff}(r) = P_0 \left[\frac{J_1(\frac{r}{r_0})}{r}\right]^2 \tag{3.15}$$

where $\mathrm{r_0} = \lambda \mathrm{L}/\pi \mathrm{D} = \mathrm{D_{Airy}}/2.44\pi$ and again the normalization constant is chosen to ensure the total area under $\mathrm{P_{diff}}$ is unity. This is well approximated by a normalized Gaussian with standard deviation $\sigma = \sqrt{1.85}\,\mathrm{r_0}$, as shown in Figure 11.

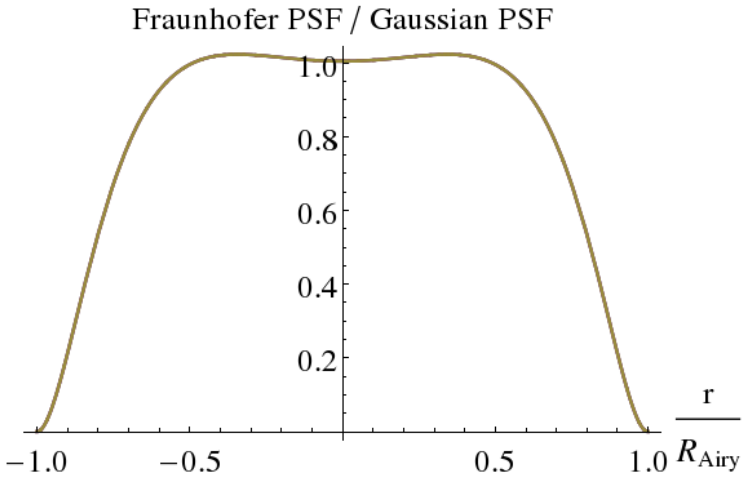

Figure 11: Ratio of the true Fraunhoffer PSF to a normalized Gaussian with $\sigma = 1.85\,r_0$, calculated for the NIF MMI with 10 μm pinholes. Results for 8, 10.2, and 13 keV exactly overlay each other.

Fresnel (near-field) Diffraction Estimates for Fresnel diffraction are less straightforward. However, estimates can be derived for the case of a circular aperture [35, 36]. Here we use the numerical algorithm described by Rees [37] to estimate the diffracted intensity profile for a pinhole located on the instrument's central axis. (See Appendix B for the Yorick code used to implement the Rees algorithm.) This calculation ignores oblique illumination; commonly, the pinholes do not reside along the central axis. The calculation could be modified to account for off-axis apertures by adding phase factors corresponding to the increased path lengths, but the fine structure of the Fresnel diffraction pattern has little effect on the final result of the PSF convolutions, as shown in Section 3.1.5.

Figures 12 - 14 show the estimated radial diffraction intensity profiles projected on the detector plane for 10, 35, and 50 μm NIF MMI pinholes, along with the Airy disk radii ($R_{Airy} \equiv 0.5\ D_{Airy}$), the radius of the blur disk ($R_{geom} \equiv 0.5\ D_{geom}$), and, in the near-field regime, the radius containing 97.6% of the radially-integrated intensity (see below). Figures 15 - 17 contain the analogous plots for the Omega MMI instrument with 5, 10, and 15 μm pinholes.

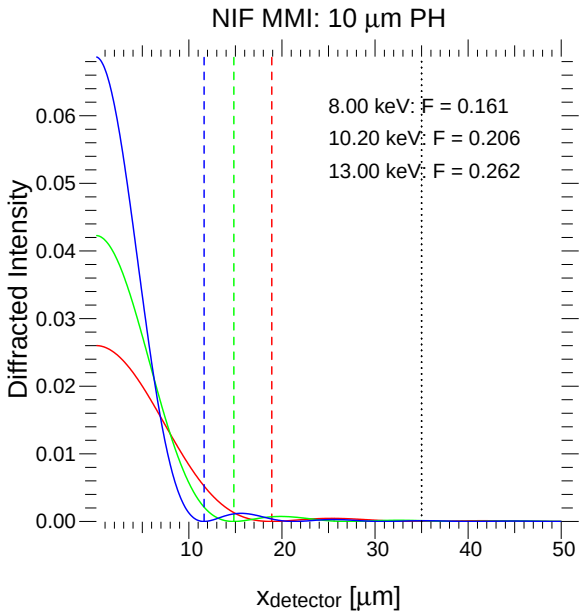

Figure 12: Radial diffraction profiles for the NIF MMI with 10 μm pinholes. Here $F \ll 1$, so Fraunhofer diffraction is plotted. Dashed lines: Airy disk radii. Dotted line (black): R_{geom}. Red: 8.0 keV; Green: 10.2 keV; Blue: 13.0 keV.

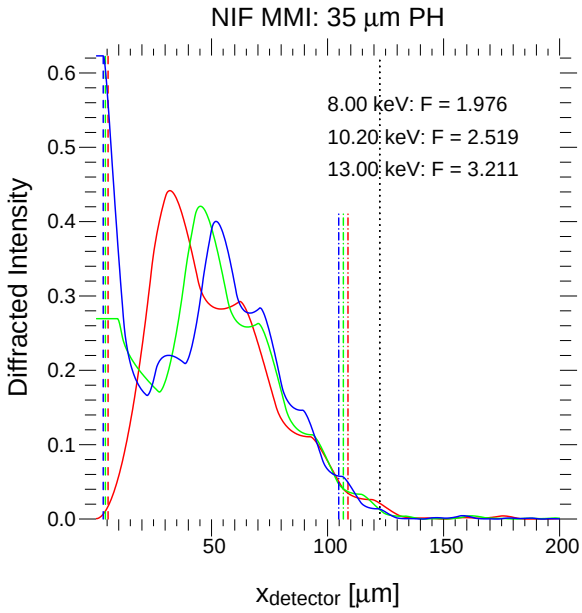

Figure 13: Radial diffraction profiles for the NIF MMI with 35 μm pinholes. Here F > 1, so Fresnel diffraction is plotted. Dashed lines: Airy disk radii. Dotted line (black): R_{geom}. Dash-dot lines: 97.6% radii (see text). Red: 8.0 keV; Green: 10.2 keV; Blue: 13.0 keV.

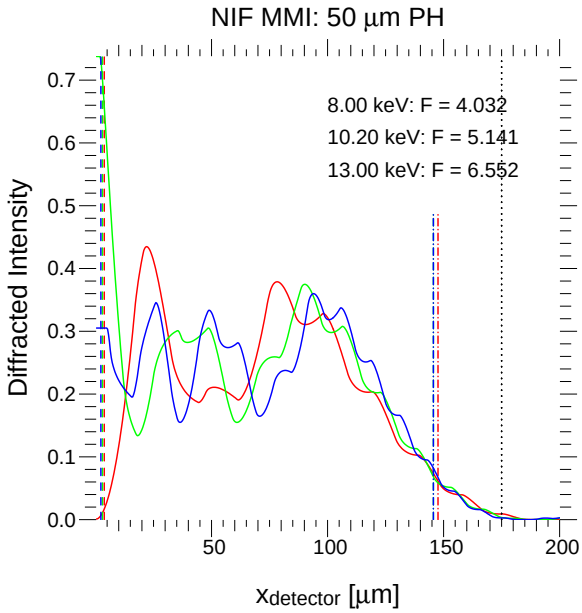

Figure 14: Radial diffraction profiles for the NIF MMI with 50 μm pinholes. Here F > 1, so Fresnel diffraction is plotted. Dashed lines: Airy disk radii. Dotted line (black): R_{geom}. Dash-dot lines: 97.6% radii (see text). Red: 8.0 keV; Green: 10.2 keV; Blue: 13.0 keV.

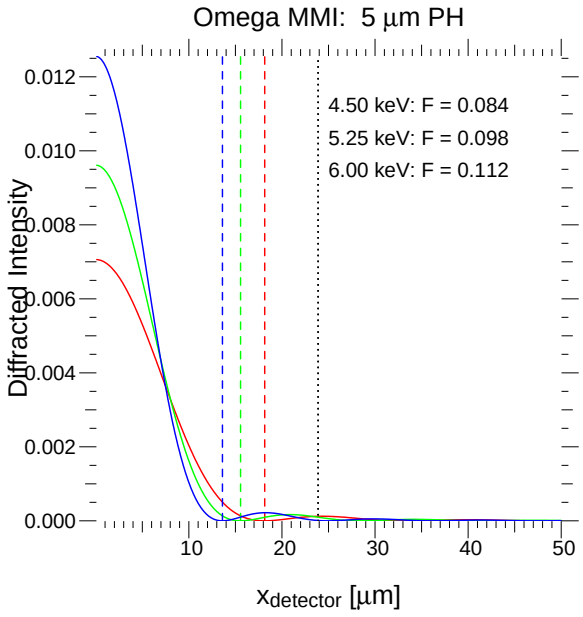

Figure 15: Radial diffraction profiles for the Omega MMI with 5 μm pinholes. Here $F \ll 1$, so Fraunhofer diffraction is plotted. Dashed lines: Airy disk radii. Dotted line (black): R_{geom}. Red: 4.5 keV; Green: 5.25 keV; Blue: 6.0 keV.

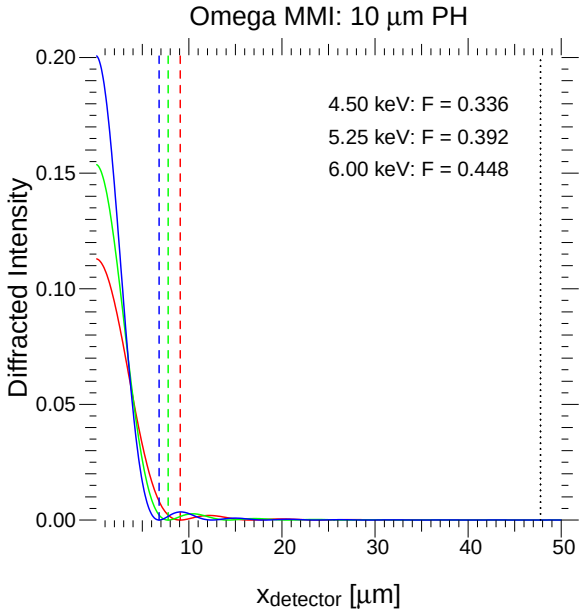

Figure 16: Radial diffraction profiles for the Omega MMI with 10 μm pinholes. Here $F \lesssim 1$, so Fraunhofer diffraction is plotted, *although the far-field assertion is debatable here.* Dashed lines: Airy disk radii. Dotted line (black): R_{geom}. Red: 4.5 keV; Green: 5.25 keV; Blue: 6.0 keV.

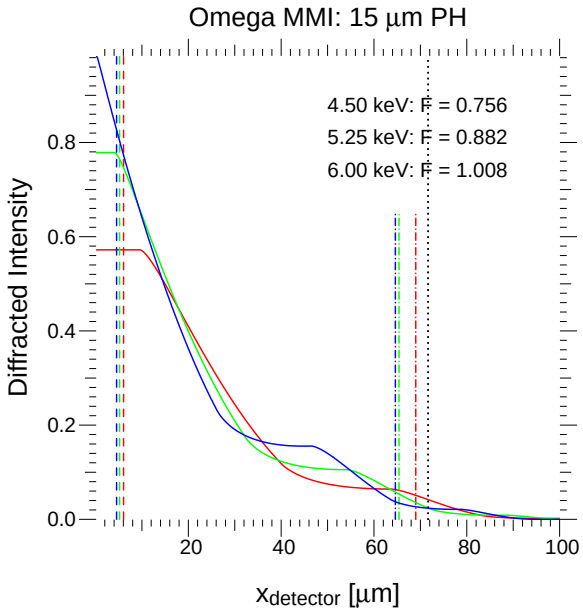

Figure 17: Radial diffraction profiles for the Omega MMI with 15 μm pinholes. Here F $\approx$ 1, so Fresnel diffraction is plotted. Dashed lines: Airy disk radii. Dotted line (black): R_{geom}. Dash-dot lines: 97.6% radii (see text). Red: 4.5 keV; Green: 5.25 keV; Blue: 6.0 keV.

(Note that in the near-field regime (F $\gtrsim$ 1), the central illumination is no longer a global maximum at all energies. This is characteristic of Fresnel diffraction [37]. Also note the Fresnel profiles are distinctly non-Gaussian.)

In all cases, the diffracted intensity falls within the geometrical blur radius, R_{geom}. Furthermore, in the near-field regime, **the Fresnel-diffracted intensity profiles extend significantly beyond the Airy disk radii**, and fall to zero only near R_{geom} (Figures 13, 14, and 17). This is to be expected; calculations at very high Fresnel numbers (F > 1000) show the diffracted intensity (or irradiance) approaches a constant function of radius until falling sharply at R_{geom} [36].

In the far-field regime, analytic integration of the Fraunhofer diffraction pattern shows the Airy disk contains approximately 97.6% of the diffracted intensity. In other words, D_{Airy} is the width of the 97.6% intensity contour. Thus, when discussing Fresnel diffraction profiles, it is useful to identify the radii that enclose 97.6% of the diffracted intensity ($R_{97.6\%}$). *This is the only way to ensure true "apples-to-apples" comparisons across both diffraction regimes.* These radii are denoted by dashed-dotted lines in Figures 13, 14, and 17. In these cases, $R_{97.6\%} \approx$ 85-95% R_{geom}.

Thus, for the purposes of Equation 3.5, a convenient energy-independent estimate for D_{diff} in the Fresnel (near-field) regime is simply $D_{diff} \approx D_{geom}$. (In this regime, $D_{geom} > D_{97.6\%} >> D_{Airy}$.)

As shown below, the fine structure in the Fresnel diffraction PSF is largely irrelevant, as it will be smeared out by convolution with the geometric shadow and detector PSFs. Thus we may approximate the Fresnel PSF by a normalized boxcar function of width D_{geom}, which is exactly the geometric shadow PSF, P_{geom}. This energy-independent (and non-Gaussian) approximation leads to excellent semi-analytic estimates for the system PSF (see Section 3.1.5).

3.1.3.3 Combined Geometric and Diffracted Contributions

The final result for the pinhole contribution to the spatial resolution varies widely, depending on whether the correct but cumbersome Equation 3.2 or the incorrect but standard Equation 3.5 is used.

Addition in Quadrature (Equation 3.5)

From above:

- In the far-field regime ($F \ll 1$), $D_{diff} = D_{Fraunhofer} \equiv D_{Airy} = \dfrac{2.44\lambda L}{D}$.
- In the near-field regime ($F \gtrsim 1$), $D_{diff} = D_{Fresnel} \equiv D_{geom} = (1 + M)\, D$.

Representative values of these D_{diff} expressions are summarized in Table 1.

NIF, 10 μm pinholes			**Omega, 5 μm pinholes**		
E [keV]	D_{Airy} [μm]	$D_{97.6\%}$ [μm]	E [keV]	D_{Airy} [μm]	$D_{97.6\%}$ [μm]
8.0	37.8	37.8	4.5[b]	36.3	36.3
10.2[a]	29.7	29.7	5.25	31.1	31.1
13.0	23.3	23.3	6.0	27.2	27.2
NIF, 35 μm pinholes			**Omega, 10 μm pinholes**		
E [keV]	D_{geom} [μm]	$D_{97.6\%}$ [μm]	E [keV]	D_{Airy} [μm]	$D_{97.6\%}$ [μm]
8.0	245.0	217.6	4.5[b]	18.2	18.2
10.2[a]	245.0	213.6	5.25	15.6	15.6
13.0	245.0	209.6	6.0	13.6	13.6
NIF, 50 μm pinholes			**Omega, 15 μm pinholes**		
E [keV]	D_{geom} [μm]	$D_{97.6\%}$ [μm]	E [keV]	D^{c}_{geom} [μm]	$D_{97.6\%}$ [μm]
8.0	350.0	295.2	4.5[b]	143.3	138.0
10.2[a]	350.0	291.2	5.25	143.3	130.8
13.0	350.0	291.2	6.0	143.3	129.2

Table 1: Diameter of the diffraction contribution to the quadature method *on the detector plane*. We define $D_{diff} \equiv D_{Airy}$ in the far-field regime and $D_{diff} \equiv D_{geom}$ in the near-field regime. [a]10.2 keV is the Ge He_α line. [b]4.76 keV is the Ti He_α line. [c]The Omega 15 μm pinhole configuration resides in the transitional regime between the near- and far-field approximations; we classify this case as belonging to the near-field regime because here the Fresnel number F = 1.01 at 6.0 keV.

Note the substantial difference between the far-field and near-field values. *The transition from the far-field to the near-field regime can increase the diffraction width by an order of magnitude.* However, the geometrical blur disk diameter, D_{geom}, exceeds $D_{97.6\%}$ in the Fresnel regime by only 4 - 20%.

In the far-field regime, the quadrature method yields a net pinhole contribution

$$D_{ph}^2 = D_{geom}^2 + D_{Airy}^2 = D_{geom}^2 + \left(\frac{2.44\lambda L}{D}\right)^2. \tag{3.16}$$

As long as the configuration remains within the far-field regime (i.e., $F \ll 1$), the error incurred by disregarding diffraction diminishes with increasing aperture size. But $F \propto D^2$, so larger apertures rapidly drive the configuration out of the far-field.

In the near-field regime, the quadrature method yields a net contribution

$$D_{ph}^2 = D_{geom}^2 + D_{geom}^2 = 2D_{geom}^2. \tag{3.17}$$

PSF Convolution (Equation 3.2)

The true pinhole PSF is given by the convolution $\mathrm{P_{geom}} * \mathrm{P_{diff}}$.

Results for the far-field regime are plotted in Figures 18-20. Although the diffraction is well-approximated by a Gaussian, the resulting pinhole PSF is *not*.

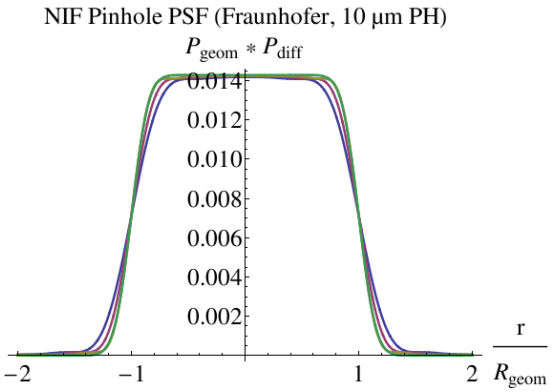

Figure 18: NIF MMI pinhole PSF in the far field (10 μm pinholes). Results using the exact (Bessel function) solutions are shown for 8 keV (blue), 10.2 keV (red), and 13 keV (yellow) alongside the Gaussian approximation for 13 keV (green).

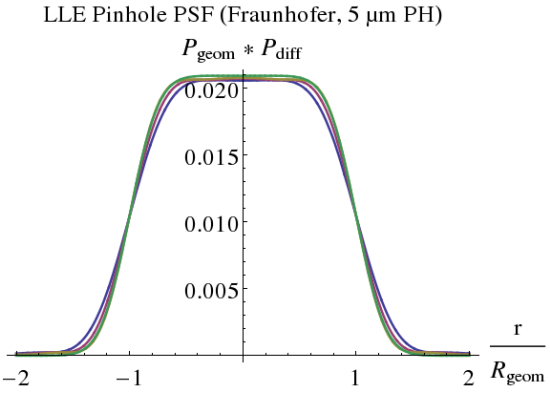

Figure 19: Omega MMI pinhole PSF in the far field (5 μm pinholes). Results using the Bessel function solutions are shown for 4.5 keV (blue), 5.25 keV (red), and 6.0 keV (yellow) alongside the Gaussian approximation for 6 keV (green).

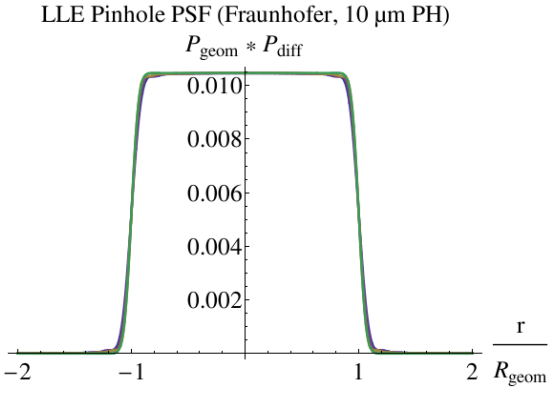

Figure 20: Omega MMI pinhole PSF in the far field (10 μm pinholes). Results using the Bessel function solutions are shown for 4.5 keV (blue), 5.25 keV (red), and 6.0 keV (yellow) alongside the Gaussian approximation for 6 keV (green).

The FWHM is $\mathrm{D_{geom}}$ in all cases. $\mathrm{R_{97.6\%}}$ resides at 1.149, 1.096, and 1.057 $\mathrm{R_{geom}}$ for

10 μm NIF pinholes (8, 10.2, and 13 keV, respectively). With 5 μm Omega pinholes, $R_{97.6\%}$ sits at 1.261, 1.204, and 1.164 R_{geom}; with 10 μm pinholes, those contours sit at 1.006, 0.9985, and 0.9930 R_{geom} (4, 5.25, and 6 keV, respectively).

The near-field pinhole PSF arises from autocorrelation of a boxcar function:

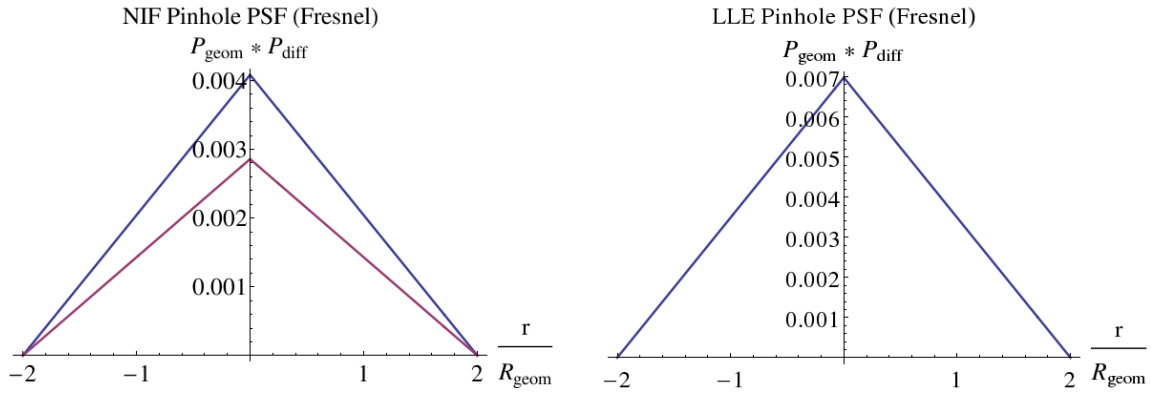

Figure 21: Left: approximate NIF MMI pinhole PSF in the Fresnel regime, calculated for 35 μm (blue) and 50 μm (red) pinholes. Right: approximate Omega MMI pinhole PSF in the Fresnel regime, calculated for 15 μm pinholes. These calculations are based on representing the Fresnel-diffraction PSF as an energy-independent boxcar with width $2R_{geom}$ (see text).

This triangular pinhole PSF is an excellent approximation for the "true" near-field pinhole PSF. This will be shown rigorously, below (see Section 3.1.5), but it is demonstrated by an exercise depicted in Figures 22 and 23.

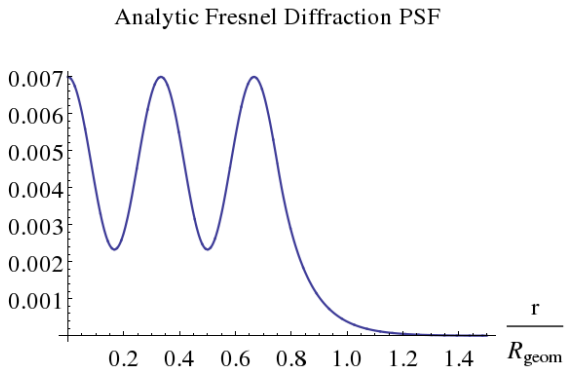

Figure 22: Analytic function representing an exaggerated Fresnel diffraction PSF. Compare Figure 14.

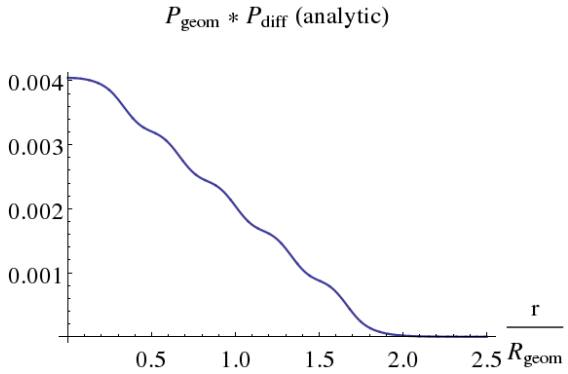

Figure 23: Convolution of the exaggerated Fresnel PSF with the geometrical shadow PSF for 35 μm pinholes. Compare Figure 21.

For the purpose of calculating an aggregate pinhole PSF, treating the Fresnel diffraction PSF as a boxcar is an excellent energy-independent approximation. When this is done, $R_{97.6\%} = 1.69\ R_{geom}$.

Recall that in the NIF far-field case, $R_{97.6\%} \approx 1.057 - 1.149\ R_{geom}$. Thus we find **the NIF pinhole PSF is effectively ∼50% - 60% wider in the near-field regime than in the far field**. Recall also that in the Omega far-field cases, we found $R_{97.6\%} \approx 1.164 - 1.261\ R_{geom}$ for 5 μm pinholes, and $R_{97.6\%} \approx 0.99 - 1.01\ R_{geom}$ for 10 μm pinholes. Thus we find **the Omega pinhole PSF is effectively ∼35% - 70% wider in the near field than in the far field.**

In summary, the aggregate pinhole PSF in the near-field (Fresnel) regime will always be significantly wider than the pinhole PSF in the far-field (Fraunhofer) regime. Estimates that incorrectly apply Frauhhofer diffraction everywhere will always underpredict the system PSF width (thereby overestimating the resolution).

Comparison of Quadratic and PSF Methods for Computing D_{ph}

Figure 24 summarizes the results for D_{ph}. In the Fraunhofer regime, the quadratic approximation (red dashes, Equation 3.5) is an acceptable estimate for the 97.6% contour width (green diamonds). In the Fresnel regime, this approximation underestimates the PSF width. It is insufficient to replace the Airy disk width with D_{geom} within the quadratic approximation (blue dashes). The aggregate pinhole contribution in the near field is correctly computed via PSF convolution (green dots).

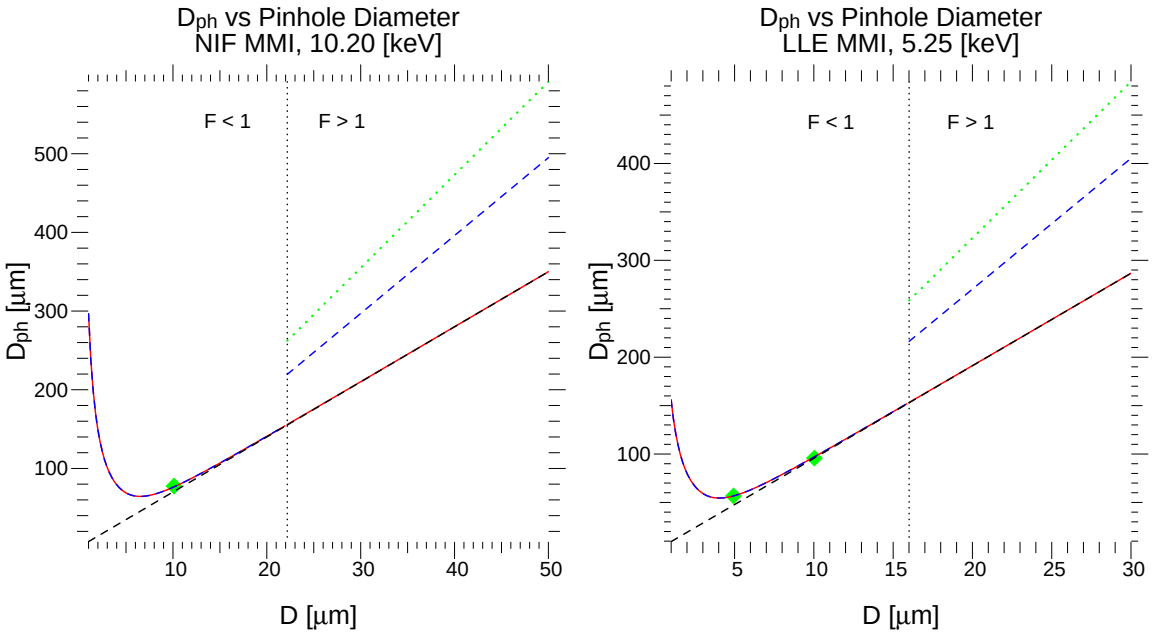

Figure 24: D_{ph} *at the detector* plotted as a function of the pinhole aperture, D, computed by several methods. Left: NIF MMI, 10.2 keV. Right: LLE MMI, 5.25 keV. Black, dashed: D_{geom}. Red: quadrature addition method with Fraunhofer diffraction assumed everywhere. Blue, dashed: quadrature addition method with Frauhofer diffraction ($D_{diff} = D_{Airy}$) applied for $F < 1$ and Fresnel diffraction ($D_{diff} = D_{geom}$) applied for $F > 1$. Green diamonds: Empirical $R_{97.6\%}$ contours derived from PSF convolution in the far-field regime, by depicting the Fraunhofer diffraction PSF as a Gaussian. Green, dotted: Analytic $R_{97.6\%}$ contours derived from PSF convolution in the near-field regime, by depicting the Fresnel diffraction PSF as a boxcar function of width D_{geom}. Black, dotted: $F = 1$. The true boundary between the far- and near-field regimes is not abrupt, but a smooth transition from $F \ll 1$ to $F \gtrsim 1$.

3.1.4 Bragg Reflector (P_{Bragg}, D_{Bragg})

A perfect monochomatic point source will not be reflected into a perfect geometrical point at the detector. The Bragg PSF arises from several causes, including imperfections in the surface finish and internal lattice dislocations.

The intensity distribution at the detector is a function of several geometrical factors. These include the angle between the incident ray and the reflector surface (typically denoted by ω in the X-ray diffraction literature); the angle between the incident ray and the direction to the detector location (commonly 2θ in the literature); and

the orientation of the diffracting plane within the Bragg lattice. (This geometry is depicted in Figure 25.) Consequently, several kinds of intensity measurements are common in the X-ray diffraction literature [38]:

- A *rocking curve* is a plot of the X-ray intensity versus ω for a fixed 2θ value.
- A *detector scan* is a plot of the X-ray intensity vs 2θ for a fixed ω value.
- A *coupled scan* is a plot of X-ray intensity vs 2θ, where $\omega = \frac{1}{2}2\theta + C_0$ and C_0 is a fixed constant offset.

Additionally, the energy-dependent reflectivity can be measured by varying the source energy while keeping ω and 2θ fixed. Monochromatic reflectivity can be measured as a function of ω via a $\omega - 2\theta$ scan (also referred to as a $\theta - 2\theta$ scan).

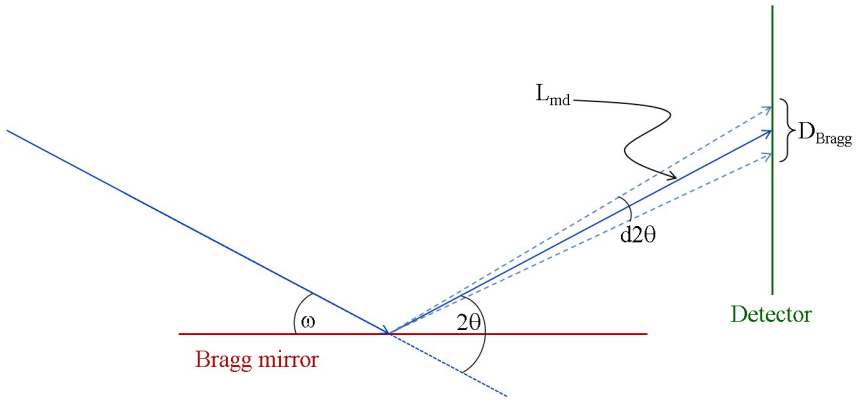

Figure 25: Geometry for estimating D_{Bragg}. Here we use definitions consistent with much of the X-ray diffraction literature (see text). The angular spread d2θ is measured by a *detector scan*.

A lower bound on D_{Bragg} comes from considering the detector-plane angular spread of a monochromatic point source shining onto the reflector via an infinitesimal pinhole. Empirically, this is approximated by a detector scan. Given suitable detector scan data, we may estimate

$$D_{Bragg} \approx L_{md} \, |d2\theta| \tag{3.18}$$

where L_{md} is the distance from the point of incidence on the mirror to the point of incidence on the detector. Unfortunately, at present, we lack empirical detector scan data for the specific W/B_4C multilayers used in the NIF and Omega MMI

instruments. Discussions of W/B_4C multilayers are common in the literature [39, 40, 41, 42, 43, 44]. However, while reflectivity measurements are prevalent in such discussions, detector scan data do not appear to be readily available.

For the multilayers installed in the NIF MMI, we have vendor-furnished calculations of the energy-dependent plane-wave reflectivity (where $C_0 = 0$ and $\omega = \theta$ is the n=1 Bragg condition) for energies between 9 and 12.5 keV [45]. For the multilayers installed in the Omega MMI instruments, we have vendor-furnished measurements of the $\theta - 2\theta$ reflectivity for the Cu K_α line (8.05 keV) [46]. Neither dataset is relevant or suitable for estimating D_{Bragg}; attempts to apply these measurements can lead to gross overestimates, as shown below in Sections 3.1.4.1 and 3.1.4.2. When estimating D_{Bragg}, it is crucial that *detector-scan data* are used.

3.1.4.1 Misestimation of D_{Bragg} from Reflectivity Data

Using plane-wave reflectivity data can give rise to anomalous estimates for D_{Bragg}, as shown here.

We start with the Bragg condition

$$n\lambda = 2d\sin\theta \tag{3.19}$$

When n=1, we have

$$E = \frac{hc}{\lambda} = \frac{hc}{2d\sin\theta} \equiv \frac{K}{\sin\theta} \tag{3.20}$$

$$\frac{dE}{d\theta} = -K\frac{\cos\theta}{\sin^2\theta}\ ; \quad |d\theta| = \left(\frac{\sin^2\theta}{\cos\theta}\right)\left(\frac{dE}{K}\right) \tag{3.21}$$

Let dθ be the angular blurring on the mirror based on the plane-wave reflectivity [45] and let

$$D_{Bragg} \approx L_{md}\,|d\theta| = L_{md}\left(\frac{\sin^2\theta}{\cos\theta}\right)\left(\frac{dE}{K}\right). \tag{3.22}$$

The interlayer spacing, d, of the W/B_4C multilayer used in the NIF MMI instrument is 1.5 nm. Thus K = 12.4 keV $\cdot$ Å/30Å = 0.413 keV. At $\theta = 2.318°$, the FWHM of the computed plane-wave reflectivity curve is 67.33 eV, which happens to be the narrowest FWHM in the 9-13 keV range. This angle corresponds to an energy E = 10.2 keV, close to the Ge He_α line. If dE = 0.06733 keV and $\theta = 2.318°$, then

$d\theta = 2.67 \times 10^{-4}$ radians at this energy. For the NIF MMI instrument, L_{md} = 63.06 cm = 6.306 $\times 10^5$ μm at the mirror center. (According to the engineering diagrams, the mirror center is situated 53.649 cm along the target/detector plane centerline, and displaced laterally 2.206 cm from that line.) Thus, for the Ge He_α line, we obtain $D_{Bragg} = 6.31 \times 10^5$ μm $\cdot$ 2.67×10^{-4} radians = 168 μm.

Empirically, D_{Bragg} is expected to be a minor factor in the instrument resolution. However, misapplying the plane-wave reflectivity data to compute D_{Bragg} overestimates its contribution to the NIF MMI resolution, putting it on par with the diffraction contribution for the smallest pinholes.

3.1.4.2 Misestimation of D_{Bragg} from $\theta - 2\theta$ Scan Data

Using $\theta - 2\theta$ reflectivity scan data can also produce anomalous estimates for D_{Bragg}, as shown here.

The W/B_4C reflectivity scan data in the Cu K_α line (8.05 keV) [46] corrsponds to an n=1 Bragg angle of 2.94°. The FWHM of the reflectivity curve at 8.05 keV is $\approx 0.75°$. For d = 1.5 nm, $E(2.94° - 0.375°) = 9.228$ keV, and $E(2.94° + 0.375°) = 7.142$ keV. This yields an extremely wide energy FWHM of approximately 2.09 keV. Similarly, using the above expression for $dE/d\theta$ with $d\theta = 0.75°$ yields an energy FWHM of 2.05 keV. If dE = 2.05 keV and $\theta = 2.94°$, then from above, $d\theta = 1.31 \times 10^{-2}$ radians in the Cu K_α line.

For the Omega MMI instrument, L_{md} = 11.7618 cm $\approx$ 1.18 $\times 10^5$ μm at the mirror center. (This value is derived from measurements performed on one of the as-built Omega MMI instruments, rather than the nominal values in the AutoCAD file [47].) Thus, if we use the $\theta - 2\theta$ data for the Cu K_α line, we get
$D_{Bragg} = 1.18 \times 10^5$ μm $\cdot$ 1.31×10^{-2} radians = 1546 μm.

Again, D_{Bragg} is expected to be relatively minor, and not a dominant factor in the instrument resolution. But misapplying the $\theta - 2\theta$ reflectivity scan data to compute D_{Bragg} makes it the dominant contribution to the Omega MMI by an order of magnitude or more.

3.1.5 System Point Spread Functions (P_{system})

By combining all known contributions, we can compute an aggregate PSF for the system (P_{system}). By taking advantage of the commutative and associative properties of convolution, as well as regime-appropriate approximations for P_{diff}, the computation of the final PSF in either diffraction regime can be turned into the convolution of a known Gaussian with a known analytic function. This can be carried out with low computational overhead using FFT methods.

In the far-field regime, the detector and Fraunhofer diffraction PSFs are both approximated as Gaussians with known variances. Their convolution is therefore also a known Gaussian. The final PSF in this regime is therefore a convolution of the composite detector-diffraction Gaussian with the boxcar function P_{geom}.

In the near-field regime, the Fresnel diffraction PSF is suitably approximated by the geometric shadow PSF, and their convolution gives rise to a known triangular function. The final PSF in this regime is therefore the convolution of this triangle with the Gaussian P_{det}.

To illustrate the effects of the various contributions, we have calculated the convolution of the numerically computed P_{diff} with P_{det}, and then the convolution of that result with P_{geom}, which gives P_{system}. We also compare the numerically computed P_{system} with the aggregate PSF derived by approximating the diffraction PSF as either a Gaussian or boxcar function, depending on the regime.

3.1.5.1 NIF

The final point spread functions for the NIF MMI are shown in Figures 26 - 28. In both regimes, using an analytic function for P_{diff} (right-side plots, dotted lines) leads to an excellent approximation of the numerically computed final system PSF (right-side plots, solid lines). Additionally, in all cases, $R_{97.6\%}$ exhibits only a weak energy dependence.

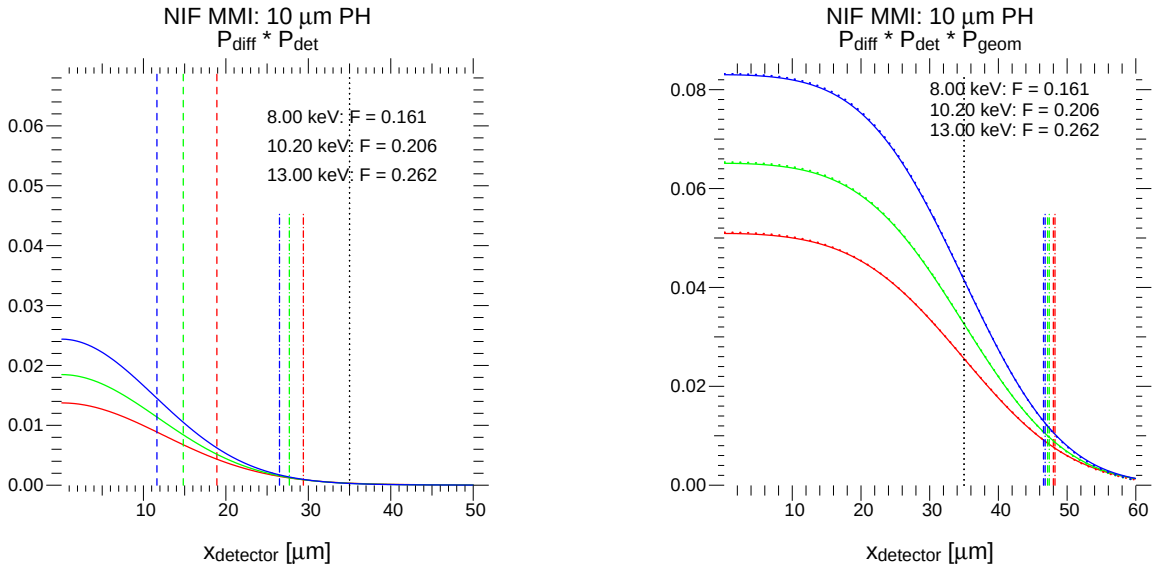

Figure 26: PSFs for 10 μm NIF MMI pinholes. Left: Numerical Fraunhofer P_{diff} (compare Figure 12) convolved with P_{det}. Dashed lines: Airy disk radii. Dash-dot lines: 97.6% contour radii. Right: P_{system}. Solid lines: Numerically computed Fraunhofer diffraction. Dotted lines: Gaussian approximation for Fraunhofer diffraction. Dashed lines: 97.6% contour radii derived from the approximated P_{diff}. Dash-dot lines: 97.6% contour radii derived from the numerical P_{diff}. Red: 8.0 keV. Green: 10.2 keV. Blue: 13.0 keV. Black (dotted line): R_{geom}.

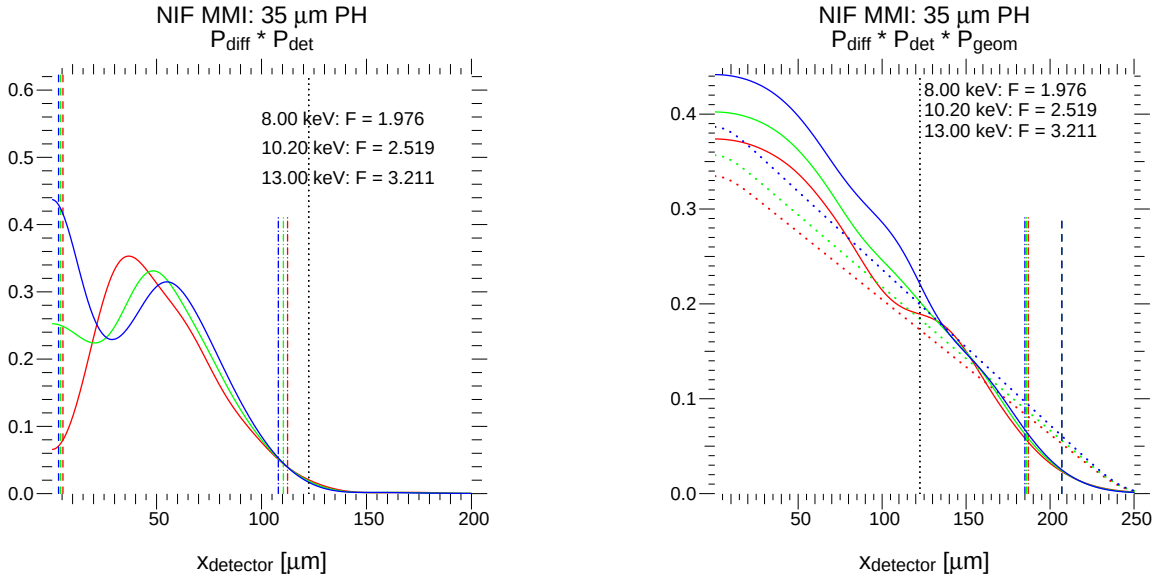

Figure 27: PSFs for 35 μm NIF MMI pinholes. Left: Numerical Fresnel P_{diff} (compare Figure 13) convolved with P_{det}. Dashed lines: Airy disk radii. Dash-dot lines: 97.6% contour radii. Right: P_{system}. Solid lines: Numerically computed Fresnel diffraction. Dotted lines: Boxcar approximation for Fresnel diffraction. Dashed lines: 97.6% contour radii derived from the approximated P_{diff}. Dash-dot lines: 97.6% contour radii derived from the numerical P_{diff}. Red: 8.0 keV. Green: 10.2 keV. Blue: 13.0 keV. Black (dotted line): R_{geom}.

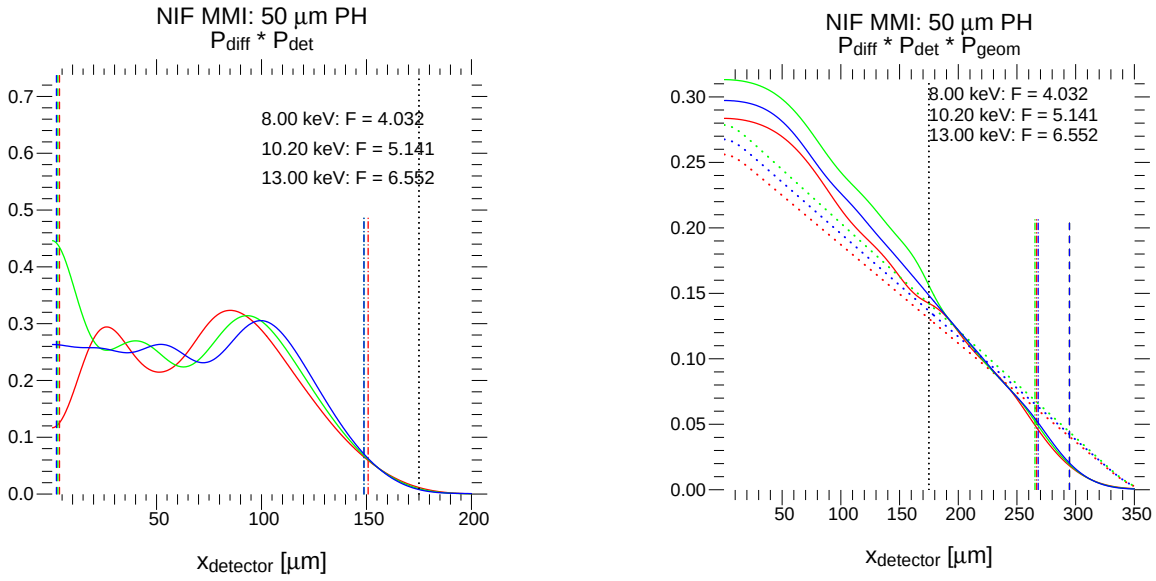

Figure 28: PSFs for 50 μm NIF MMI pinholes. Left: Numerical Fresnel P_{diff} (compare Figure 14) convolved with P_{det}. Dashed lines: Airy disk radii. Dash-dot lines: 97.6% contour radii. Right: P_{system}. Solid lines: Numerically computed Fresnel diffraction. Dotted lines: Boxcar approximation for Fresnel diffraction. Dashed lines: 97.6% contour radii derived from the approximated P_{diff}. Dash-dot lines: 97.6% contour radii derived from the numerical P_{diff}. Red: 8.0 keV. Green: 10.2 keV. Blue: 13.0 keV. Black (dotted line): R_{geom}.

3.1.5.2 Omega

The final point spread functions for the Omega MMI are shown in Figures 29 - 31. As with the P_{system} calculations for the NIF MMI, we find $R_{97.6\%}$ exhibits a very weak energy dependence. Using an analytic function for P_{diff} yields an excellent approximation for the numerically computed final system PSF when the diffraction resides firmly in the far- or near field regime. As expected, the approximation may be less effective in the transitional regime, such as where D = 15 μm. The approximated Fresnel diffraction PSF was applied to that case (in keeping with Figure 17), though the Fraunhofer approximation may be equally effective there.

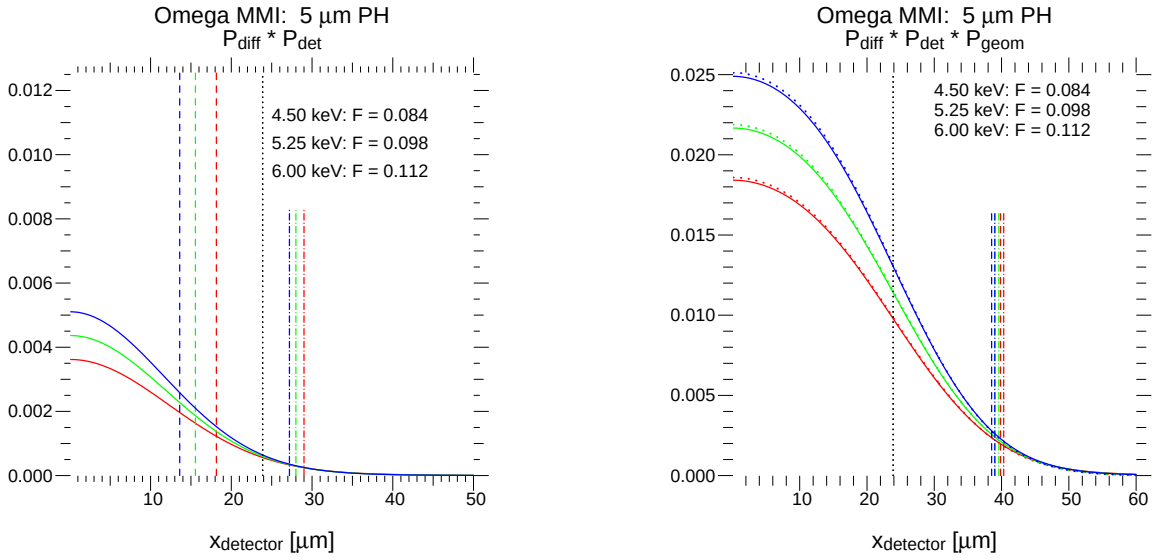

Figure 29: PSFs for 5 μm Omega MMI pinholes. Left: Numerical Fraunhofer P_{diff} (compare Figure 15) convolved with P_{det}. Dashed lines: Airy disk radii. Dash-dot lines: 97.6% contour radii. Right: P_{system}. Solid lines: Numerically computed Fraunhofer diffraction. Dotted lines: Gaussian approximation for Fraunhofer diffraction. Dashed lines: 97.6% contour radii derived from the approximated P_{diff}. Dash-dot lines: 97.6% contour radii derived from the numerical P_{diff}. Red: 4.5 keV. Green: 5.25 keV. Blue: 6.0 keV. Black (dotted line): R_{geom}.

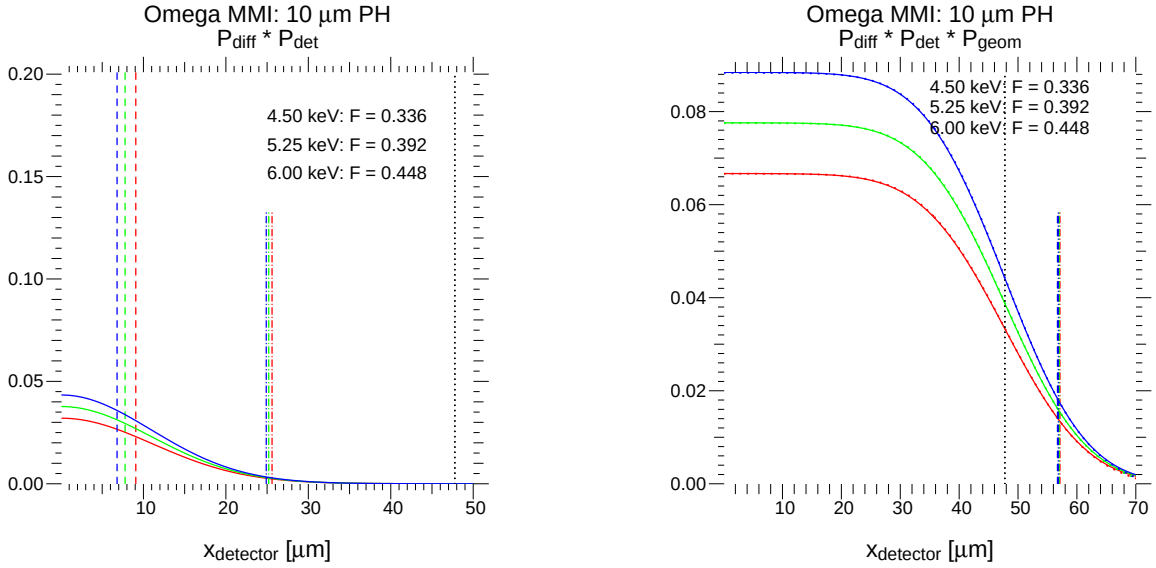

Figure 30: PSFs for 10 μm Omega MMI pinholes. Left: Numerical Fraunhofer P_{diff} (compare Figure 16) convolved with P_{det}. Dashed lines: Airy disk radii. Dash-dot lines: 97.6% contour radii. Right: P_{system}. Solid lines: Numerically computed Fraunhofer diffraction. Dotted lines: Gaussian approximation for Fraunhofer diffraction. Dashed lines: 97.6% contour radii derived from the approximated P_{diff}. Dash-dot lines: 97.6% contour radii derived from the numerically P_{diff}. Red: 4.5 keV. Green: 5.25 keV. Blue: 6.0 keV. Black (dotted line): R_{geom}.

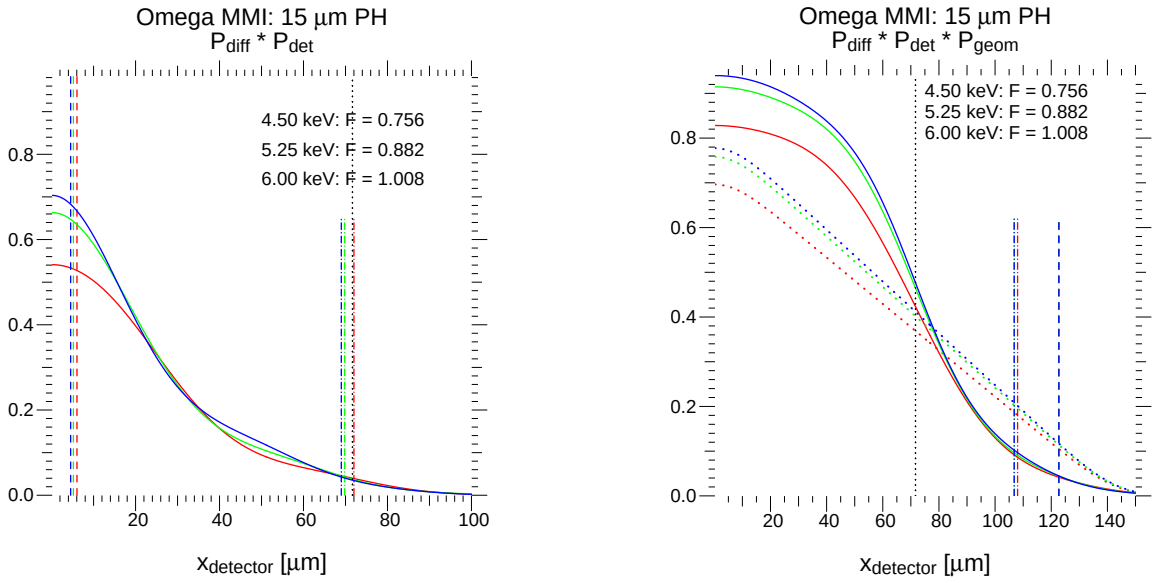

Figure 31: PSFs for 15 μm Omega MMI pinholes. Left: Numerically Fresnel P_{diff} (compare Figure 17) convolved with P_{det}. Dashed lines: Airy disk radii. Dash-dot lines: 97.6% contour radii. Right: P_{system}. Solid lines: Numerically computed Fresnel diffraction. Dotted lines: Boxcar approximation for Fresnel diffraction. Dashed lines: 97.6% contour radii derived from the approximated P_{diff}. Dash-dot lines: 97.6% contour radii derived from the numerical P_{diff}. Red: 4.5 keV. Green: 5.25 keV. Blue: 6.0 keV. Black (dotted line): R_{geom}.

3.1.6 Resolution Estimates

The analytic function convolutions can be used to place a lower bound on the size of a monochromatic point source on the MMI image plane. (A lower bound because, lacking data, the present calculations cannot account for the Bragg contribution.) In particular, we compute the width of the 97.6% contour for P_{system}. For comparison, we can also compute $D_{x,y}$ using the quadature addition method. Owing to the weak energy dependence of $R_{97.6\%}$, as demonstrated in Section 3.1.5, it is sufficient to examine the system resolution at a single energy.

Table 2 summarizes the results for the NIF MMI resolution *at the source* given a Ge He$_\alpha$ (10.2 keV) point source. The results were obtained by several methods: numerically (PSF convolution with no approximations); semi-analytically, approximating the diffraction PSFs; and via the quadrature method. The detector-plane sizes are obtained by multiplying these values by the instrument magnification, M = 6.

D [μm]	**$D_{97.6\%}$ [μm] (PSF; numeric.)**	**$D_{97.6\%}$ [μm] (PSF; approx.)**	**$D_{x,y}$ [μm] (Quadrature; far- & near-field)**	**$D_{x,y}$ [μm] (Quadrature; far-field only)**	**$D_{x,y}$ [μm] (Quadrature; no diffraction)**
10^a	>15.8	>15.7	>15.2	>15.2	>14.3
35^b	>62.0	>69.0	>58.3	>41.7	>41.7
50^b	>88.4	>98.2	>82.9	>58.9	>58.9

Table 2: NIF MMI resolution *at the source* for a monochromatic Ge He_α point source. The calculation in the second column applied convolutions to the numerically calculated diffraction profiles. The calculation in the third column approximated the diffraction PSFs with analytic functions. The quadrature estimate in the fourth column accounted for the distinction between Fraunhofer and Fresnel diffraction, per Equations 3.16 and 3.17. The fifth column contains the results from incorrectly applying Fraunhofer diffraction, regardless of the diffraction regime, to the quadrature estimate. Values in the sixth column were obtained by disregarding diffraction entirely. [a]Far-field regime. [b]Near-field regime.

In the far field, the error in the analytic approximation is less than 1%, while the quadrature method yields 4% error when including diffraction, and 10% error when disregarding it. In the near field, the analytic approximation produces an 11% overestimate, while the regime-aware quadrature method *using* $P_{diff} = P_{geom}$ produces only a 6% underestimate, compared to a 30% underestimate when diffraction is disregarded or the incorrect (far-field) regime applied.

It is useful to consider the area of an independent resolution element (see Section 4). The resolved area is $A_{res} = \frac{\pi}{4} D^2_{97.6\%}$ or $A_{res} = \frac{\pi}{4} D_x D_y$, as appropriate.

D [μm]	**A_{res} [μm^2] (PSF; numeric.)**	**A_{res} [μm^2] (PSF; approx.)**	**A_{res} [μm^2] (Quadrature; far- & near-field)**	**A_{res} [μm^2] (Quadrature; far-field only)**	**A_{res} [μm^2] (Quadrature; no diffraction)**
10	>200	>190	>180	>180	>160
35	>3020	>3740	>2670	>1370	>1360
50	>6140	>7570	>5400	>2730	>2730

Table 3: Area *at the source* of the resolved ellipse of a Ge He_α point source.

Similarly, we can place a lower bound on the size of a monochromatic 5.25 keV point source on the Omega MMI image plane. Table 4 summarizes the results for the resolution *at the source plane* (the detector plane resolutions are obtained by multiplying these values by the instrument magnification, M = 8.6), and Table 5 summarizes estimates for the area of the resolved ellipse, A_{res}.

D [μm]	**$D_{97.6\%}$ [μm] (PSF; numeric.)**	**$D_{97.6\%}$ [μm] (PSF; approx.)**	**$D_{x,y}$ [μm] (Quadrature; far- & near-field)**	**$D_{x,y}$ [μm] (Quadrature; far-field only)**	**$D_{x,y}$ [μm] (Quadrature; no diffraction)**
5[a]	>9.3	>9.1	>8.9	>8.9	>8.1
10[a]	>13.3	>13.3	>12.7	>12.7	>12.6
15[b]	>25.0	>28.7	>24.4	>17.8	>17.7

Table 4: Omega MMI resolution *at the source* for a monochromatic 5.25 keV point source. The calculation in the second column applied convolutions to the numerically calculated diffraction profiles. The calculation in the third column approximated the diffraction PSFs with analytic functions. The quadrature estimate in the fourth column accounted for the distinction between Fraunhofer and Fresnel diffraction, per Equations 3.16 and 3.17. The fifth column contains the results from incorrectly applying Fraunhofer diffraction, regardless of the diffraction regime, to the quadrature estimate. Values in the sixth column were obtained by disregarding diffraction entirely. [a]Far-field regime. [b]Near-field regime.

D [μm]	**A_{res} [μm^2] (PSF; numeric.)**	**A_{res} [μm^2] (PSF; approx.)**	**A_{res} [μm^2] (Quadrature; far- & near-field)**	**A_{res} [μm^2] (Quadrature; far-field only)**	**A_{res} [μm^2] (Quadrature; no diffraction)**
5	>70	>70	>60	>60	>50
10	>140	>140	>130	>130	>120
15	>490	>650	>470	>250	>250

Table 5: Area *at the source* of the resolved ellipse for a monochromatic 5.25 keV point source.

Results here are similar to those for the NIF MMI. In the far field, the error in the analytic approximation is less than 3%, while the quadrature method yields 4% error when including diffraction, and 5-12% error when disregarding it. In the near field, the analytic approximation produces a 15% overestimate, while the regime-aware quadrature method *using* $P_{diff} = P_{geom}$ produces only a 2% underestimate, compared to a 30% underestimate when diffraction is disregarded or the incorrect (far-field) regime applied.

We should expect the quadrature method to perform well in this scenario, because we have explicitly chosen to represent the unknown detector PSF by a Gaussian. Numerical experiments using a Lorentzian form for P_{det} (while maintaining the same FWHM) find the regime-aware quadrature method performs significantly worse in the far field ($\approx$ 19 - 30% error for NIF and Omega, respectively, as opposed to $\approx$ 4%), but not significantly differently in the near field. Furthermore, these results do not account for P_{Bragg}, which may have a non-Gaussian form.

3.2 Spectral Resolution

Let the strip length of the framing camera be L_s microns. If one complete MMI image covers a fraction f_s of that strip for the full energy domain, then a simple estimate for the energy variation along the strip is

$$\frac{dE}{dL} = \frac{(E_{max} - E_{min})}{f_s L_s} \text{ [keV } \mu\text{m}^{-1}] \tag{3.23}$$

The maximum spectral resolution, R_e is this value times the *detector plane* spatial resolution in the energy direction, D_x or $D_{97.6\%}$. The energy resolution of a single detector element is this value times D_{det}.

3.2.1 NIF

The nGXI2-000-000 camera has a maximum strip length of 39.42 mm = 3.942 cm [48]. (This is the length measured in the timing direction of the strip, which for the NIF MMI is also the energy direction.) If one complete MMI image uses 60% of the strip [49], then a single image convering the NIF MMI energy domain has

$$\frac{dE}{dL} = \frac{13.0 - 8.0 \text{ keV}}{0.60 \cdot 3.942 \times 10^4 \ \mu\text{m}} = 2.11 \times 10^{-4} \text{ [keV } \mu\text{m}^{-1}] = 0.211 \text{ [eV } \mu\text{m}^{-1}]. \tag{3.24}$$

Using $D_{det} = 50$ μm, as above, we deduce the spectral resolution of a single element on the MCP is roughly 0.211 eV $\mu\text{m}^{-1} \cdot 50$ μm pixel^{-1} = 10.6 eV pixel^{-1}. Estimates for R_e are listed in Table 6.

D [μm]	R_e **[eV] (PSF; numeric.)**	R_e **[eV] (PSF; approx.)**	R_e **[eV] (Quadrature; far- & near-field)**	R_e **[eV] (Quadrature; far-field only)**	R_e **[eV] (Quadrature; no diffraction)**
10	>20.0	>19.9	>19.2	>19.2	>18.1
35	>78.5	>87.4	>73.8	>52.8	>52.8
50	>111.9	>124.3	>105.0	>74.6	>74.6

Table 6: NIF MMI spectral resolution *at the detector plane*. These values are based on spatial resolution estimates for a Ge He_α point source from Section 3.1.6.

According to George Kyrala [50] the resolving power of the NIF MMI is

$$\frac{E}{\Delta E} = \frac{10\text{keV}}{75\text{eV}} \approx 133.$$

3.2.2 Omega

According to Scott Hsu [17], the Omega X-ray framing cameras have a photocathode length of approximately 34 mm. According to Taisuke Nagayama [27], the resolving power of the Omega MMI is

$$\frac{E}{\Delta E} \approx 150.$$

According to Roberto Mancini [51], the spectral resolution of the Omega MMI instruments using 10 μm pinholes with the W/B_4C multilayer Bragg reflectors is 20 eV.

4 Constraints on the Signal Level

Given the preceding analyses of the MMI photonics budget (Section 2) and spatial resolution (Section 3), we can derive meaningful constraints on the signal level, S (see Section 2.1).

4.1 Photon Statistics and the Resolvable Contrast Between Image Elements

It is possible to derive a simple relationship between the number of detected photons and the resolvable contrast between two adjacent image elements. We begin by summarizing an analysis by Tom Murphy [52, 53].

Consider a pair of adjacent image elements with equal area, A μm^{-2}. Let (detected) photons fall on element 1 with a density of n photons μm^{-2}, and let the the density of detected photons on element 2 be n$(1-\delta)$ photons μm^{-2}. Here δ is the contrast between elements. Then the total number of photons on element 1 is $\mathrm{N}_1 = \mathrm{nA}$, and the total number of photons on element 2 is $\mathrm{N}_2 = \mathrm{n}(1-\delta)\mathrm{A}$.

For these image elements to be individually resolvable, the absolute difference in their detected photons must exceed the statistical uncertainty in the difference. If the photon distribution is dominated by Poisson noise, as expected when the signal level is low, the statistical uncertainty in the number of photons for each individual element is

$$\sigma_{N_1} = \sqrt{N_1} = \sqrt{nA} \tag{4.1}$$

$$\sigma_{N_2} = \sqrt{N_2} = \sqrt{n\left(1-\delta\right)A} \tag{4.2}$$

The absolute difference is simply

$$\Delta N = N_1 - N_2 = nA - nA\left(1-\delta\right) = nA\delta \tag{4.3}$$

while the statistical uncertainty in the difference is given by

$$\sigma_{\Delta N} = \sqrt{\left(\frac{\partial \Delta N}{\partial N_1}\right)^2 \sigma_{N_1}^2 + \left(\frac{\partial \Delta N}{\partial N_2}\right)^2 \sigma_{N_2}^2} = \sqrt{\sigma_{N_1}^2 + \sigma_{N_2}^2} = \sqrt{nA\left(2-\delta\right)}. \tag{4.4}$$

Thus, if these elements are to be independently resolvable, we require $\Delta \mathrm{N} > \sigma_{\Delta \mathrm{N}}$, or

$$nA\delta > \sqrt{nA\,(2-\delta)} \implies nA > \frac{2-\delta}{\delta^2}. \tag{4.5}$$

Recall that nA is the total number of detected photons falling on element 1, i.e., on the brighter of the two image elements. Thus nA is equivalent to the number of photons detected per independent resolution element, $\mathrm{N_d}$, which was derived in Section 2.2. We may obtain the minimum resolvable contrast, δ_{min}, as a function of the detected photons, $\mathrm{N_d}$:

$$N_d = \frac{2-\delta_{min}}{\delta_{min}^2} \implies \delta_{min} = \frac{-1+\sqrt{1+8N_d}}{2N_d} \tag{4.6}$$

where we have disregarded one solution owing to the requirement that $\delta > 0$. This expression tells us that if an element receives $\mathrm{N_d}$ (detected) photons, the contrast with its neighbor must exceed δ_{min} in order for those adjacent resolution elements to be resolvable.

The resolution constraint on $\mathrm{N_d}$ is plotted in figure 32, and the minimum contrast, δ_{min}, is plotted in Figure 33. (Recall that larger δ values correspond to larger brightness differences between adjacent elements, by virtue of $1-\delta$.)

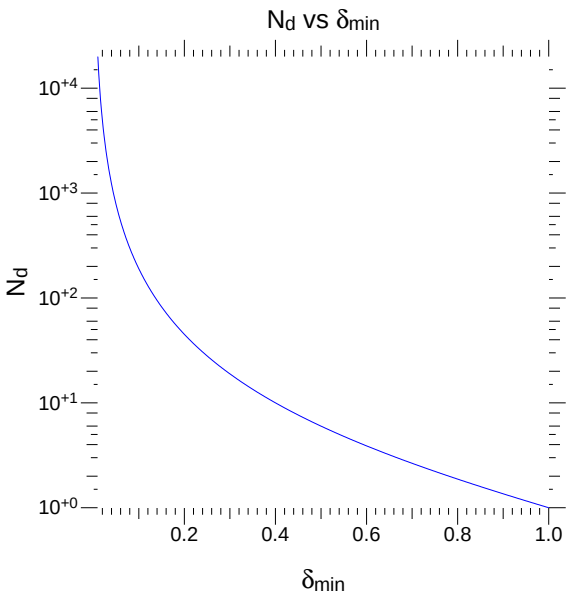

Figure 32: $\mathrm{N_d}$ as a function of minimum resolvable contrast, δ_{min}.

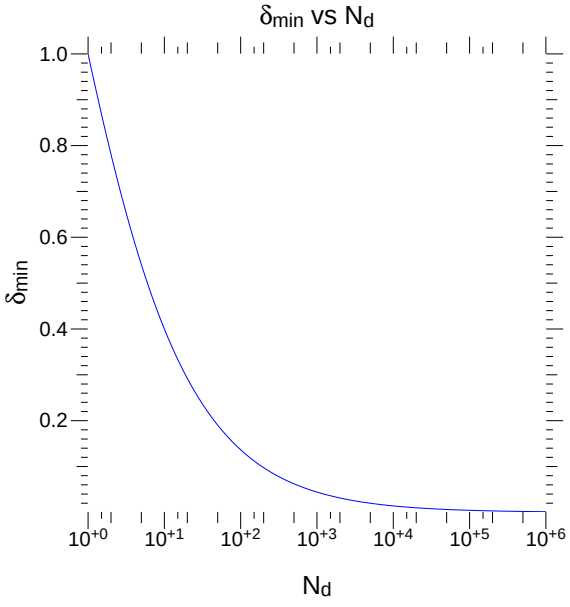

Figure 33: Minimum resolvable contrast, δ_{min}, as a function of $\mathrm{N_d}$.

4.2 Relationship Between Signal Level (S) and Resolution

In the preceding discussion, we used n to denote the number of detected photons falling per square micron. This is exactly the quantity $N_{\mu m^2}$ derived in Section 2.2. We can therefore write the following requirement for adjacent resolution elements to be independently resolvable:

$$N_{\mu m^2} A > \frac{2-\delta}{\delta^2} \implies A^* \equiv \frac{2-\delta}{N_{\mu m^2} \cdot \delta^2}. \tag{4.7}$$

Here A^* is the minimum area of an image element such that it can be independently resolved from its neighbors at contrast level δ, owing to Poisson statistical fluctuations, given an areal density of detected photons $N_{\mu m^2}$. In other words, A^* is the minimum collecting area of a resolution element such that it will accumulate sufficient photons to reduce the fluctuations below the level at which adjacent elements will be resolvable with contrast δ.

From Section 2.2, $N_{\mu m^2}$ is known as a function of the signal level, burn width, and various properties of the instrument. Namely, by combining equations 2.7 and 2.15,

$$N_{\mu m^2} = 6.242 \times 10^{15} \left(\frac{S \cdot \Delta E_{eV} \cdot \Delta g_{ps}}{\Delta b_{ps} \cdot A_{\mu m^2} \cdot \delta E_{keV}} \right) \cdot \frac{\pi D^2}{4 L_{tp}^2 M^2} \cdot \eta \ [\text{photon} \cdot \mu\text{m}^{-2}] \tag{4.8}$$

or

$$N_{\mu m^2} \equiv S \cdot G \left(\Delta g_{ps}, \Delta b_{ps}, \Delta E_{eV}, \delta E_{keV}, A_{\mu m^2}, M, D, L_{tp}, \eta \right). \tag{4.9}$$

Thus we can write A^* as an explicit function of the signal level, S:

$$A^* \equiv \frac{1}{S} \left(\frac{2-\delta}{G \cdot \delta^2} \right) \tag{4.10}$$

From Section 3, we know the *inherent size* of an independent resolution element (i.e., determined by the instrument properties) is

$$A_{res} = \frac{\pi}{4} D_x D_y$$

and perhaps $D_x = D_y = D_{97.6\%}$ depending upon the calculation method. Thus, for a given contrast level δ:

- When $A^* < A_{res}$, the resolution is determined by the inherent properties of the instrument.

- When $A^* > A_{res}$, the resolution is limited by photon statistics.

We therefore seek the minimum signal level S_{min} such that $A^* < A_{res}$. Our condition on A^* becomes

$$\frac{1}{S_{min}}\left(\frac{2-\delta}{G\cdot\delta^2}\right) = A^* < \frac{\pi}{4}D_xD_y$$

or

$$S_{min} = \frac{4\,(2-\delta)}{G\pi D_x D_y \delta^2}\ [\mathrm{J}\cdot\mathrm{eV}^{-1}\cdot\mathrm{sr}^{-1}] \tag{4.11}$$

where

$$G = 6.242\times10^{15}\left(\frac{\Delta E_{eV}\cdot\Delta g_{ps}}{\Delta b_{ps}\cdot A_{\mu m^2}\cdot\delta E_{keV}}\right)\cdot\frac{\pi D^2}{4L_{tp}^2M^2}\cdot\eta\ [\mathrm{photon}\cdot\mathrm{sr}\cdot\mathrm{eV}\cdot\mathrm{J}^{-1}\cdot\mu\mathrm{m}^{-2}]. \tag{4.12}$$

For a given contrast level, δ, S_{min} is the signal level at which the minimum size of a *statistically* resolvable image element is smaller than the instrument's *inherent* resolution element size. In other words:

- **When $S > S_{min}$, the resolution is determined by the instrument properties.**

- **When $S < S_{min}$, the image is dominated by photon statistics.**

Because $S_{min} \propto D^{-2}$, S_{min} grows as the pinhole diameter decreases. This is to be expected: if the pinhole size decreases while everything else is held constant, the image will become dimmer and thus noisier, owing to Poisson fluctuations. So the signal must increase in order to prevent photon statistics from swamping the image.

Note also that because $S_{min} \propto (D_x D_y)^{-1}$, underestimating the diffraction contribution to the PSF width (e.g., by disregarding it entirely, or by mistakenly applying Fraunhofer diffraction estimates to the near-field regime) will increase S_{min}.

This derivation considers only Poisson noise. Additional noise will increase S_{min}.

4.3 Examples: S_{min} Estimates for the NIF MMI

S_{min} depends upon specific properties of the instrument, some of which are energy dependent, as well as details of the experiment: the burn width, the area of the

emitting region, and so forth. For the purposes of the following examples we take the burn width (Δb_{ps}) to be 100 ps, the gating time (Δg_{ps}) to be 70 ps, and the pinhole bandwidth (ΔE_{eV}) to be 100 eV. We also take $\eta_{MCP} = 0.07$ and estimate $\eta_{Bragg} \sim 0.30$. We include a Kapton blast shield of 2.5 mm. We take the pixel size to be 50 μm. The target-pinhole plane distance for the NIF MMI, L_{tp}, is 16.667 cm $= 1.6667 \times 10^5 \mu$m.

As noted above, the total number of photons available to the detector depends upon the area of the emitting region, $A_{\mu m^2}$. In what follows, we apply the results from sections 2 and 3 as appropriate to compute $N_{\mu m^2}$, N_{pix}, D_x, D_y, etc.

4.3.1 Uniformly Mixed Hot Dopant

Consider the case where the emitting dopant is uniformly mixed through a core 300 μm in diameter. Via Equations 2.7, 2.16, 4.11, and 4.12 we derive the following:

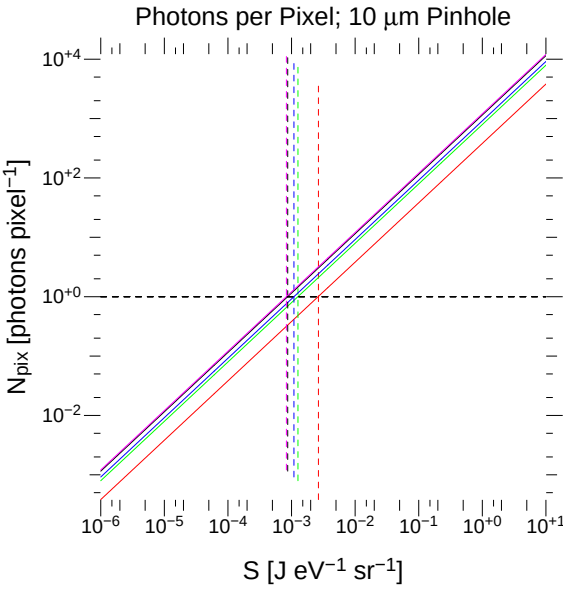

Figure 34: Photons per pixel vs signal, for uniform emission. Signal levels such that $N_{pix} = 1$ are marked with dashed lines. Red: 8.0 keV; Green: 9.6 keV; Blue: 10.2 keV; Black: 12.0 keV; Magenta: 13.0 keV.

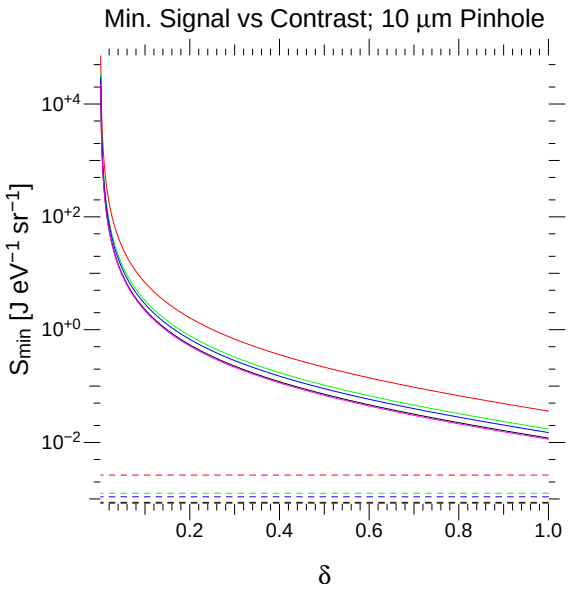

Figure 35: Minimum signal level vs contrast, for uniform emission. Image resolution is dominated by photon statistics for signals below the solid curves. Signal levels such that $N_{pix} = 1$ are marked with dashed lines.

We see that for a 10 μm pinhole, the small size of the resolution element forces S_{min} high enough that the number of photons detected per pixel will always exceed unity. However, the high S_{min} levels required may be unattainable, in which case the images will always be dominated by photon statistics, even at the highest contrast levels.

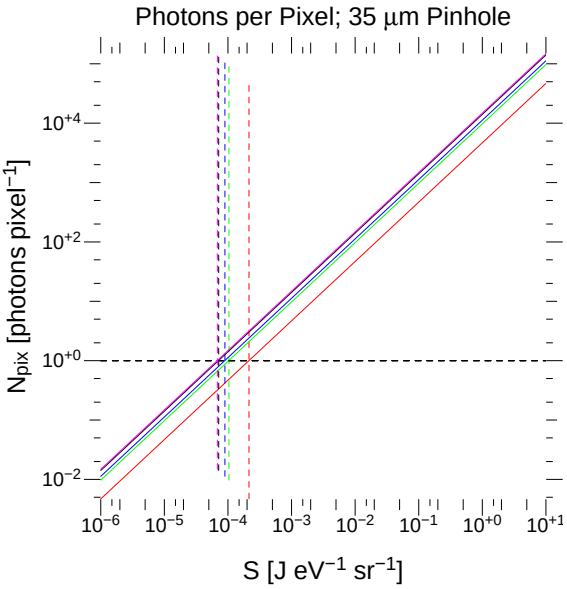

Figure 36: Photons per pixel vs signal, for uniform emission. Signal levels such that $N_{pix} = 1$ are marked with dashed lines. Red: 8.0 keV; Green: 9.6 keV; Blue: 10.2 keV; Black: 12.0 keV; Magenta: 13.0 keV.

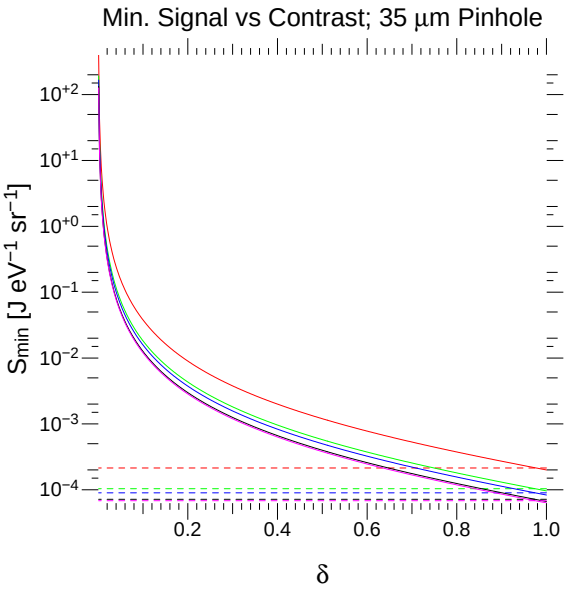

Figure 37: Minimum signal level vs contrast, for uniform emission. Image resolution is dominated by photon statistics for signals below the solid curves. Signal levels such that $N_{pix} = 1$ are marked with dashed lines.

As expected, the signal levels required to avoid photon statistics are lower for 35 μm pinholes than for 10 μm pinholes. Furthermore, the requirement that every pixel receives at least one photon (which is a very weak lower bound on the intensity; other considerations may place tighter lower bounds) constrains the signal only at the very highest contrast levels.

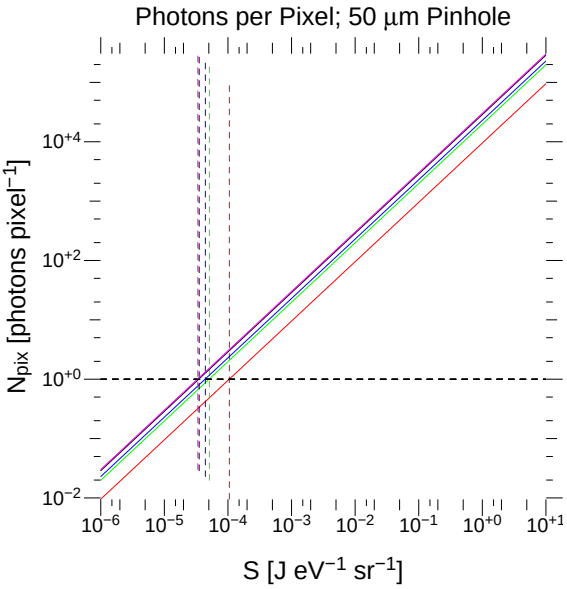

Figure 38: Photons per pixel vs signal, for uniform emission. Signal levels such that $N_{pix} = 1$ are marked with dashed lines. Red: 8.0 keV; Green: 9.6 keV; Blue: 10.2 keV; Black: 12.0 keV; Magenta: 13.0 keV.

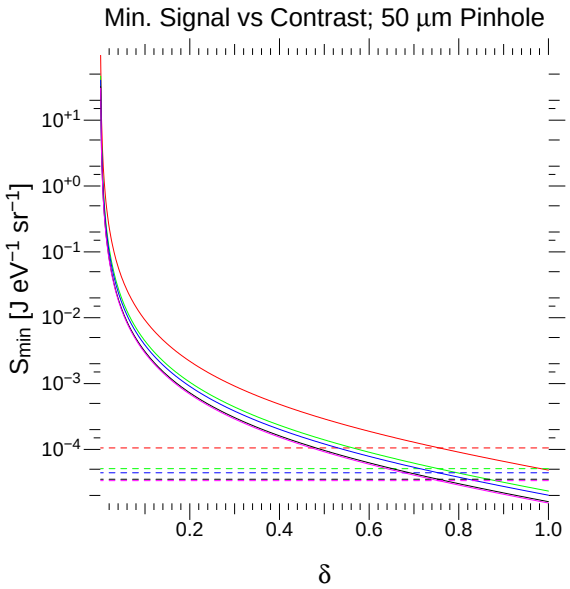

Figure 39: Minimum signal level vs contrast, for uniform emission. Image resolution is dominated by photon statistics for signals below the solid curves. Signal levels such that $N_{pix} = 1$ are marked with dashed lines.

When the pinhole diameter is 50 μm, the required signal levels are lower still, but now the requirement that every pixel receive at least one photon puts an additional constraint on the signal. For instance, constrast levels above $\sim 70\%$ are not resolvable when $S = S_{min}$ and thus require higher signal levels.

4.3.2 Hot Dopant Mixed into a Shell of Thickness 10 μm

Now consider the case where the hot core is still 300 μm in diameter, but the emitting dopant is mixed into a thin 10 μm region surrounding the core. In this case, the emitting area $A_{\mu m^2}$ is considerably smaller than in the uniformly mixed case. As seen in figures 40 - 45, we see trends similar to those found above in the uniformly mixed case, but the thresholds are lower because $S_{min} \propto A_{\mu m^2}$.

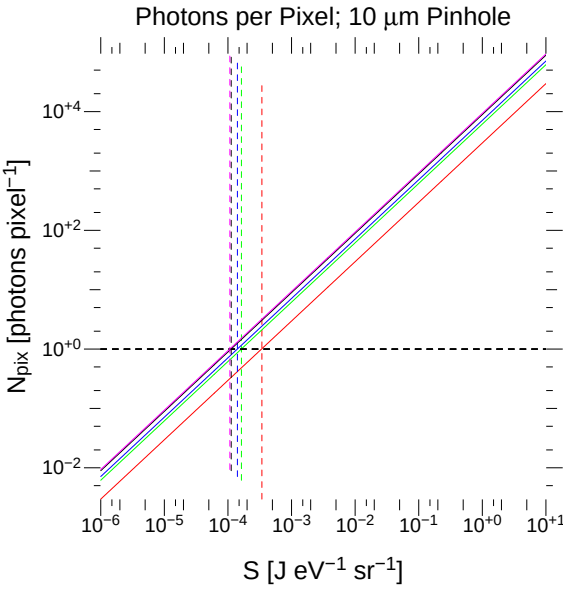

Figure 40: Photons per pixel vs signal, for emission confined to a 10 μm region. Signal levels such that $N_{pix} = 1$ are marked with dashed lines. Red: 8.0 keV; Green: 9.6 keV; Blue: 10.2 keV; Black: 12.0 keV; Magenta: 13.0 keV.

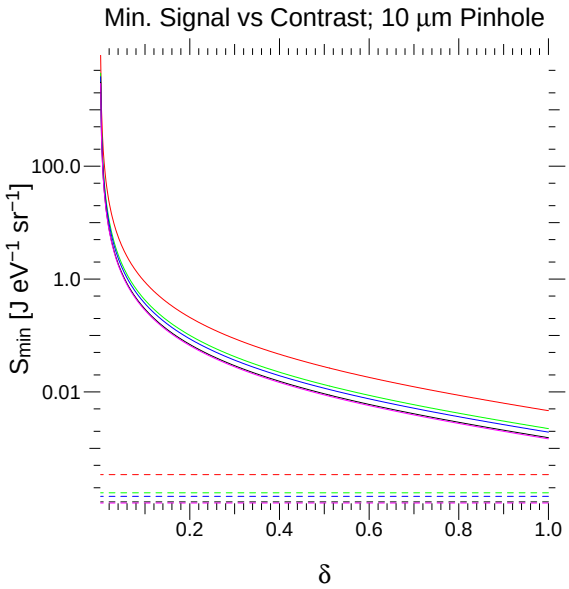

Figure 41: Minimum signal level vs contrast, for emission confined to a 10 μm region. Image resolution is dominated by photon statistics for signals below the solid curves. Signal levels such that $N_{pix} = 1$ are marked with dashed lines.

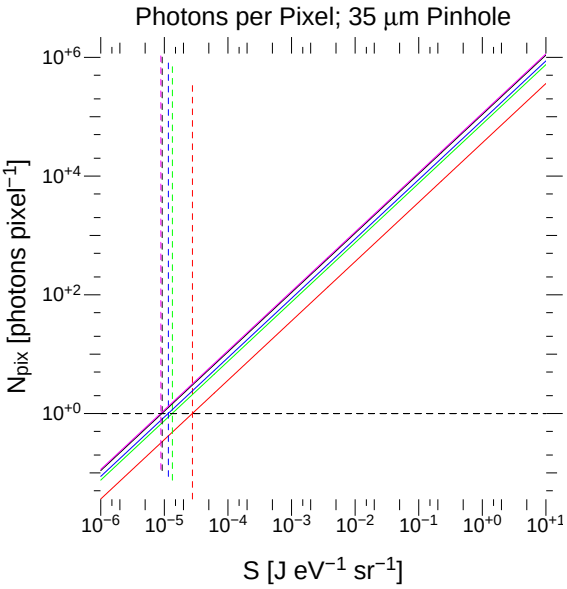

Figure 42: Photons per pixel vs signal, for emission confined to a 10 μm region. Signal levels such that $N_{pix} = 1$ are marked with dashed lines. Red: 8.0 keV; Green: 9.6 keV; Blue: 10.2 keV; Black: 12.0 keV; Magenta: 13.0 keV.

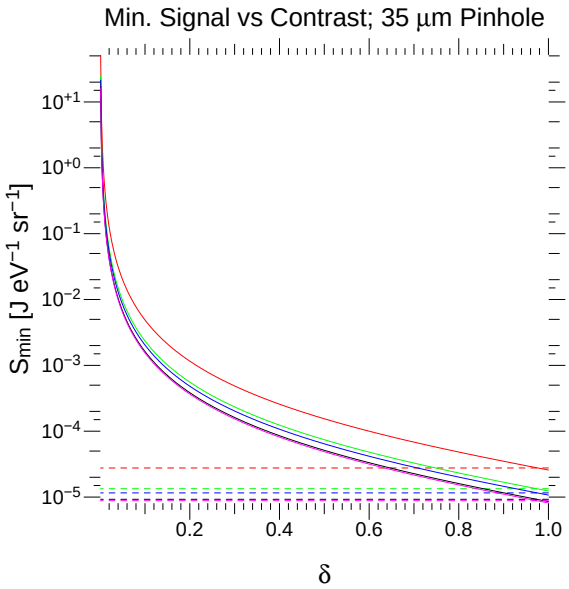

Figure 43: Minimum signal level vs contrast, for emission confined to a 10 μm region. Image resolution is dominated by photon statistics for signals below the solid curves. Signal levels such that $N_{pix} = 1$ are marked with dashed lines.

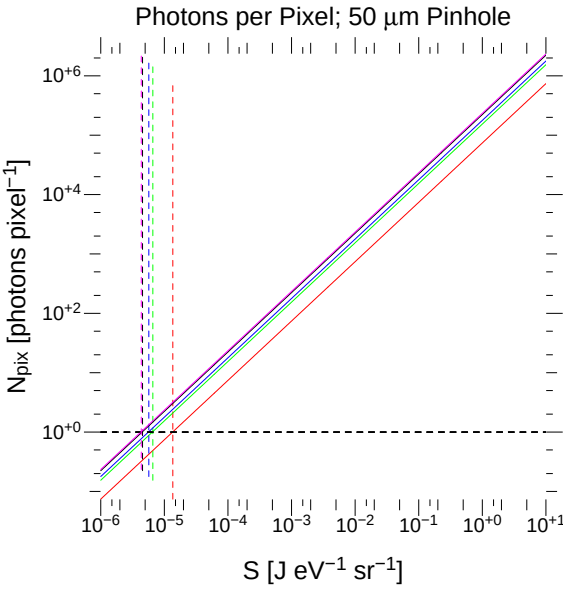

Figure 44: Photons per pixel vs signal, for emission confined to a 10 μm region. Signal levels such that $N_{pix} = 1$ are marked with dashed lines. Red: 8.0 keV; Green: 9.6 keV; Blue: 10.2 keV; Black: 12.0 keV; Magenta: 13.0 keV.

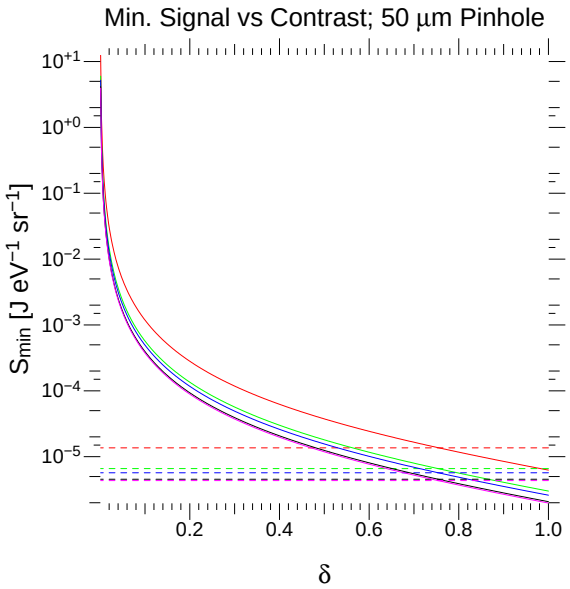

Figure 45: Minimum signal level vs contrast, for emission confined to a 10 μm region. Image resolution is dominated by photon statistics for signals below the solid curves. Signal levels such that $N_{pix} = 1$ are marked with dashed lines.

4.3.3 NIF Shot N121119

The Ge He$_\alpha$ signal measured by the NIF Supersnout-II instrument for shot N121119 was approximately [15] 6.2 J keV^{-1} sr^{-1} or 6.2×10^{-3} J eV^{-1} sr^{-1} (see the example calculation in Section 2.1). Furthermore, George Kyrala has estimated [15] the emission in that line corresponded to 6.2×10^{-5} J keV^{-1} sr^{-1} μm^{-2}, which suggests the effective emitting area, $A_{\mu m^2}$ was $\sim 10^5$ μm^2.

This is below the stated NIF MMI specification for signal detectability, 8×10^{-4} J keV^{-1} sr^{-1} μm^{-2} [54]. Yet a spectral line feature is clearly visible in strips 2 and 3 (and perhaps strip 1) of the raw MMI hGXI (MCP) image, as shown in Figure 46.

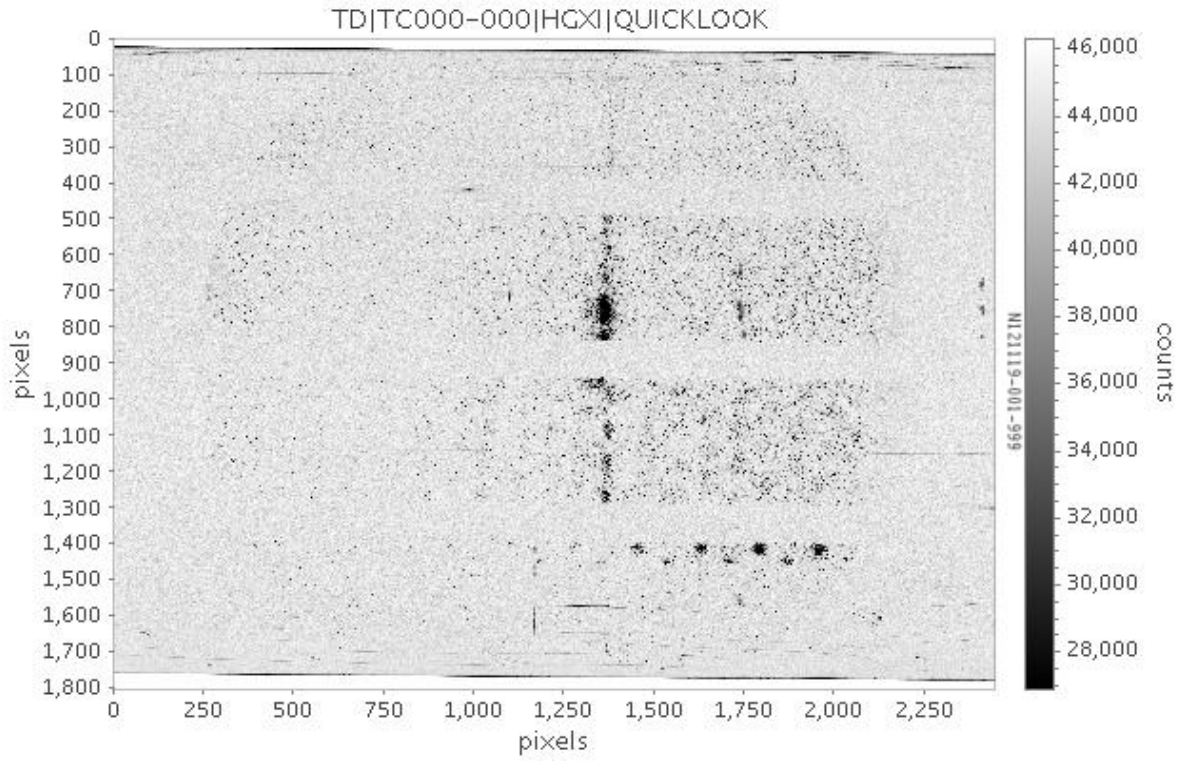

Figure 46: Raw MMI hGXI (multichannel plate) image for NIF shot N121119. Strips 2 and 3 contain a clear feature corresponding to the strongest emission line, Ge He_α (10.2 keV); the line is faintly visible in strip 1 (top). Strip 4 (bottom) corresponds to a later time.

The appearance of such a feature is unexpected based on the stated threshold for detectability. Indeed, when we compute S_{min} as a function of contrast for this case ($A_{\mu m^2} \sim 10^5$ μm^2, and assuming $\Delta E_{eV} = 100$, $\Delta b_{ps} = 100$, $\Delta g_{ps} = 70$), we conclude this level of Ge He_α emission is not resolvable with 10 μm pinholes at any contrast level. (The detected signal level in this case corresponds to approximately 4 photons per pixel, or a signal-to-noise ratio of 2.) However, we find it should be resolvable with 35 μm pinholes for $\delta > 18\%$. In this case, the detected signal level corresponds to 2.0×10^{-2} photons μm^{-2}, or approximately 49 photons per pixel (i.e., a signal-to-noise ratio of 7).

This analysis is plotted in figures 47 - 52.

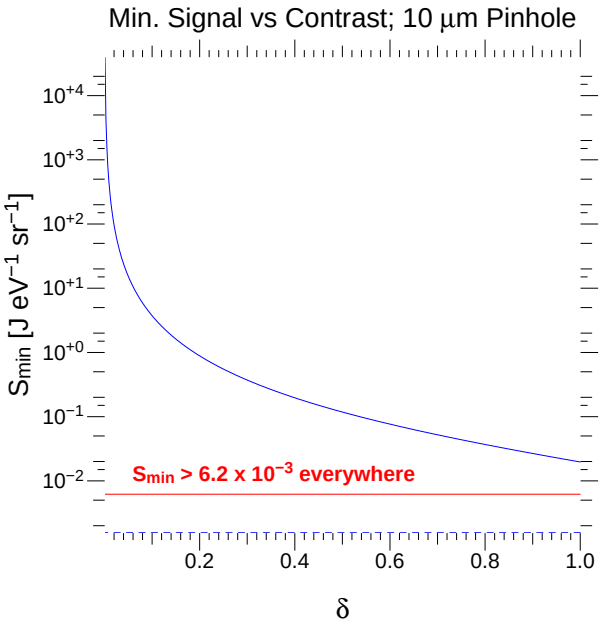

Figure 47: Minimum signal level as a function of contrast in the Ge He_α line (10.2 keV), for NIF shot N121119 with 10 μm pinholes. The estimated signal level for this shot, S = 6.2×10^{-3} J eV^{-1} sr^{-1}, falls below the resolvability threshold at all contrast levels.

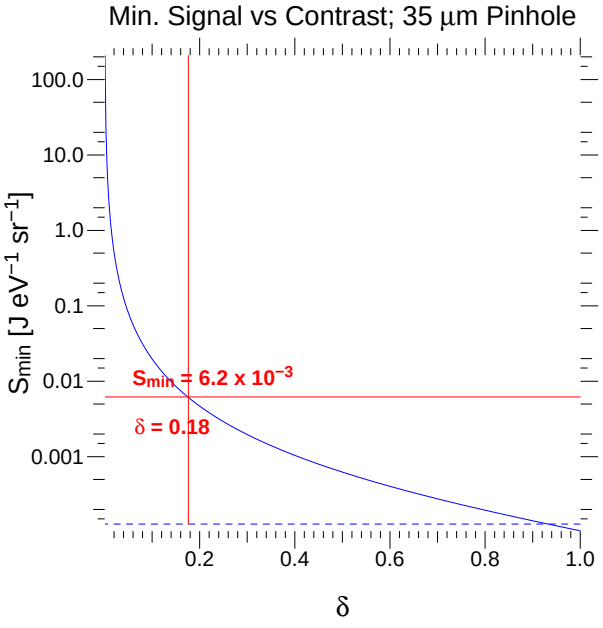

Figure 48: Minimum signal level as a function of contrast in the Ge He_α line (10.2 keV), for NIF shot N121119 with 35 μm pinholes. The estimated signal level for this shot, S = 6.2×10^{-3} J eV^{-1} sr^{-1}, exceeds the resolvability threshold S_{min} as long as the contrast, δ, exceeds 18%.

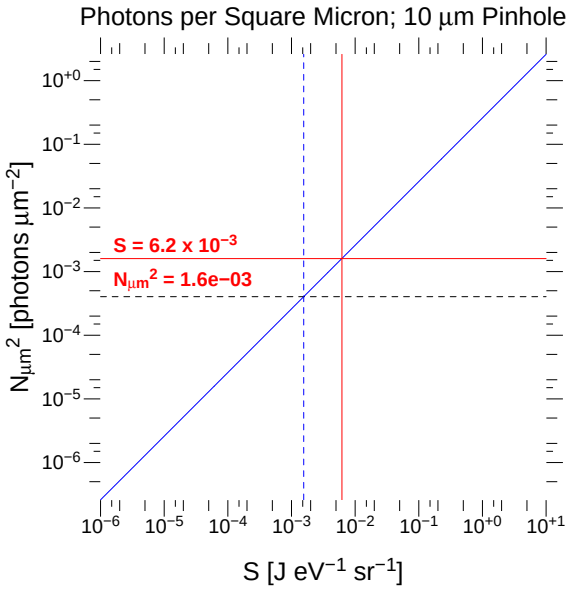

Figure 49: Detected photons per square micron in the Ge He$_\alpha$ line (10.2 keV), for NIF shot N121119 with 10 μm pinholes.

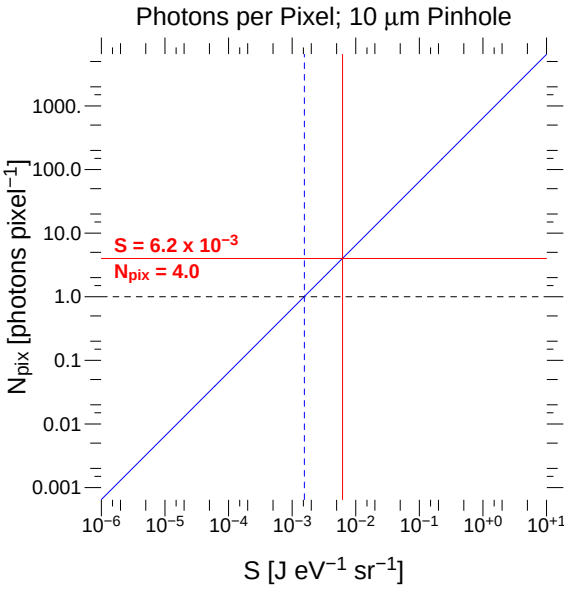

Figure 50: Detected photons per pixel in the Ge He$_\alpha$ line (10.2 keV), for NIF shot N121119 with 10 μm pinholes.

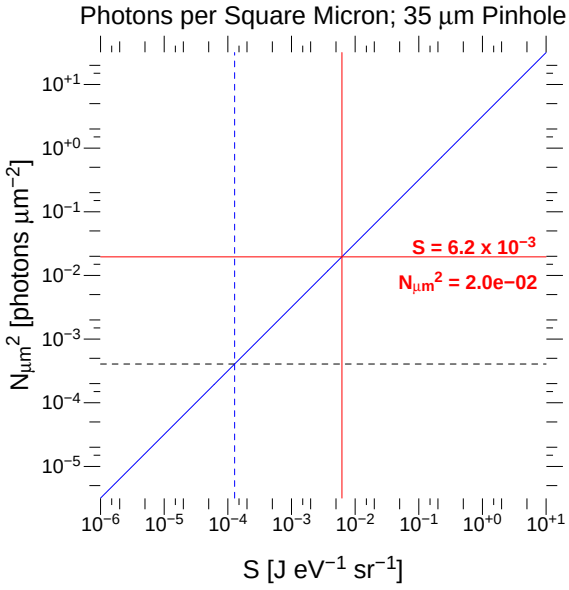

Figure 51: Detected photons per square micron in the Ge He$_\alpha$ line (10.2 keV), for NIF shot N121119 with 35 μm pinholes.

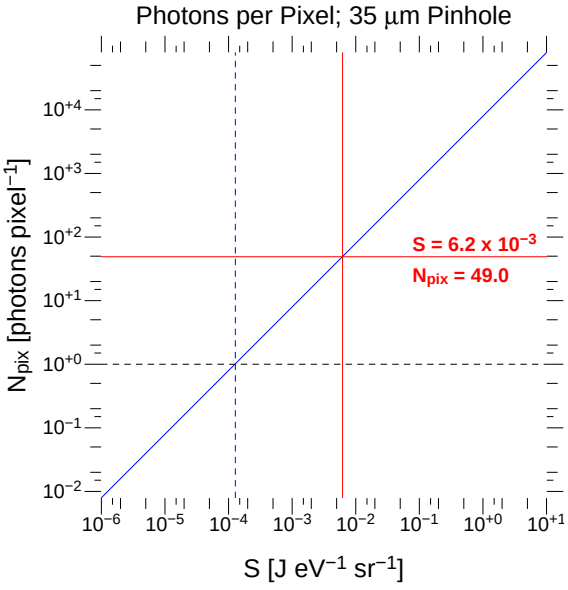

Figure 52: Detected photons per pixel in the Ge He$_\alpha$ line (10.2 keV), for NIF shot N121119 with 35 μm pinholes.

5 Summary

The mean number of photons detected per unit area of the MMI image plane (Equations 2.14 - 2.16) is a function of several quantities including the emission signal level (S), the étendue of the imaging system, the burn width, the gating period, and the bandwidth of the individual pinhole images. The bandwidth will vary across the detector plane, and may be considerable ($\gtrsim$ 100 eV). This nonmonochromaticity arises from the finite sizes of both the pinhole and source, although source size is the dominant factor by an order of magnitude.

The spatial resolution of the instrument is properly derived from a calculation of the monochromatic point spread function (PSF) image width. In practice, spatial resolution estimates are commonly obtained by adding the contributing function widths in quadrature. However, this approach is only mathematically valid when all contributing functions are Gaussian and the half-widths are equated with the associated standard deviations. Yet the geometrical shadow (ray optics) PSF is highly non-Gaussian and cannot be approximated as such, so the quadrature method is, technically, never valid. Nevertheless, under very particular circumstances, the quadrature method may yield decent estimates, as explained below.

When estimating the diffraction contribution, it is crucial to assess the regime, i.e., whether the instrument resides in the near- or far field for scalar diffraction theory. (In fact, as shown in Section 3.1.3.2, a single instrument may inhabit different regimes at different energies, depending upon its configuration.) Far-field (Fraunhofer) and near-field (Fresnel) diffraction are substantially different. The Fraunhofer diffraction PSF is adequately approximated as a Gaussian. The Fresnel PSF is adequately approximated by the geometrical shadow (ray optics) PSF, which is a boxcar.

In the far field, estimates of the diffraction contribution from a circular aperture typically and sensibly refer to the Airy disk width. (This is the basis of the Rayleigh resolution criterion.) But this width is a useful fiducial because it contains nearly all the flux transmitted through the aperture: approximately 97.6%. Therefore, in any analysis which inherently refers to the Airy disk when in the far-field regime, the only way to ensure true "apples-to-apples"comparisons of different contributions is to compare the widths of the 97.6% flux contours. This is the most consistent method of comparing and measuring PSF widths.

Resolution estimates which disregard diffraction can be highly inaccurate, particularly when the system resides in the near field. Resolution estimates that mistakenly apply the Fraunhofer estimate to the Fresnel regime are no better. This is a common error, because the Fraunhofer (Airy disk) width decreases with increasing aperture size as D^{-1}, which leads to the misconception that diffraction may be disregarded for larger pinholes. However, the dimensionless Fresnel number $\mathrm{F} \propto \mathrm{D}^2$, which means the far-field diffraction regime becomes irrelevant faster than it becomes negligible. The near field (Fresnel) diffraction width is proportional to D, not D^{-1}.

Correct calculation of the final system PSF width requires numerical or analytic estimates for the diffraction, detector, and Bragg mirror PSFs, which subsequently must be convolved. Namely,

$$P_{system}(r) = P_{ph}(r) * P_{Bragg}(r) * P_{det}(r) .$$

When using this approach, the pinhole PSF is itself the convolution of geometric ($\mathrm{P_{geom}}$) and diffraction ($\mathrm{P_{diff}}$) contributions, where

- $\mathrm{P_{geom}}$ is a boxcar function of width $\mathrm{D_{geom}}$ (see below).
- $\mathrm{P_{diff}}$ depends on F, the Fresnel number for the system (Equation 3.9), which varies as a function of energy and aperture size:
  - When $\mathrm{F} \ll 1$, pinhole diffraction resides in the far-field (Fraunhofer) regime, in which case $\mathrm{P_{diff}}$ can be approximated as a Gaussian with standard deviation $\sigma = \sqrt{1.85}\ \mathrm{D_{Airy}}/2.44\pi$.
  - When $\mathrm{F} \gtrsim 1$, pinhole diffraction is more appropriately described by the near-field (Fresnel) regime, in which case a simple but effective energy-independent approximation is $\mathrm{P_{diff}} = \mathrm{P_{geom}}$.

The PSF convolution technique may be cumbersome or infeasible. In that case, one may obtain acceptable estimates via the quadrature method if the detector and Bragg mirror contributions can be justifiably modeled as Gaussians, and *if the diffraction contribution is treated properly.*

In that situation, the width of the monochromatic point spread function (PSF) *on the detector* is estimated by

$$D_{x,y}^2 \approx D_{det}^2 + D_{ph}^2 + D_{Bragg}^2 \approx D_{det}^2 + D_{geom}^2 + D_{diff}^2 + D_{Bragg}^2$$

where

- D_{det} is an inherent aggregate property of the detector (e.g., 50 μm).
- D_{geom} is the diameter of the geometrical blur disk from ray optics: $(1 + M)\, D$.
- D_{diff} again depends on F:
  - When $F \ll 1$ (the far-field regime)

$$D_{diff} = D_{Airy} = \frac{2.44 \lambda L}{D}$$

  - When $F \gtrsim 1$ (the near-field regime)

$$D_{diff} \approx D_{geom} = (1 + M)\, D$$

- D_{Bragg} can be estimated from good detector-scan data for the relevant crystal or multilayer reflector, but other types of scan datasets may lead to gross overestimates. When lacking detector-scan data, D_{Bragg} may be omitted to obtain a lower bound on $D_{x,y}$.

The PSF width relative to the source is $D_{x,y}/M$.

By considering the resolvable contrast between adjacent image elements, and applying this to the mean number of detected photons per unit area, it is possible to define the minimum area of an image element, A^*, such that it may be resolved from its neighbors at a given contrast level, δ (Equation 4.7). Comparison of A^* and the area of the detector-plane PSF leads to a simple expression for S_{min}, the minimum acceptable signal level of emission (Equations 4.11 - 4.12).

- When $S > S_{min}$, the image resolution is determined by the instrument properties, rather than photon statistics.
- When $S < S_{min}$, the image is dominated by photon (Poisson) statistics.

This S_{min} analysis is consistent with the detection of Ge He_α emission by the NIF MMI on shot N121119, which occurred despite emission in that line falling an order of magnitude below the instrument's design specification for signal detectability.

A Relationship Between Energy and Position on the Pinhole Plane

It is often useful to relate a position on the MMI pinhole plane to an energy at the detector plane. For an MMI instrument with flat Bragg mirrors (such as those fielded at NIF and Omega), the relevant geometry can be depicted with a simple cartoon:

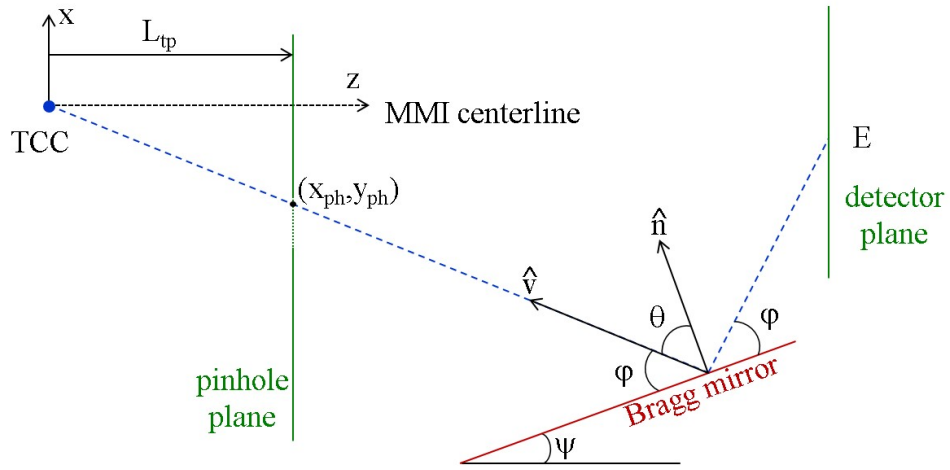

Figure 53: Geometrical relationship between position on the pinhole plane and energy on the detector plane.

Here the central axis of the instrument lies in the z-direction; the pinhole plane is orthogonal to this and located at $z = L_{tp}$ (L_{tp} is the distance from target chamber center (TCC) to the pinhole plane). A geometrical ray from the capsule (located at the origin, TCC) passes through the pinhole plane at (x_{ph}, y_{ph}) to impinge on the Bragg reflector with incidence angle φ, which corresponds to an energy E at the detector. We seek to understand how E varies as a function of x_{ph} and y_{ph}. For the purposes of this discussion it is sufficient to assume ideal n=1 Bragg reflection.

Let $\hat{n}$ denote the unit vector normal to the mirror surface at the point where the ray impinges, and let $\hat{v}$ denote the unit vector from the mirror along the ray through the

pinhole plane toward TCC. Then

$$E = \frac{hc}{2d\sin\varphi} \equiv \frac{K}{\sin\varphi} = \frac{K}{\sin\left(\frac{\pi}{2} - \theta\right)} = \frac{K}{\cos\theta} = \frac{K}{\hat{n}\cdot\hat{v}}. \tag{A.1}$$

Given

$$\hat{n} = (n_x, n_y, n_z) \tag{A.2}$$

$$\hat{v} = -\frac{(x_{ph}, y_{ph}, L_{tp})}{\sqrt{x_{ph}^2 + y_{ph}^2 + L_{tp}^2}} \tag{A.3}$$

we obtain the following equation for E as a function of x_{ph} and y_{ph}:

$$E = \frac{-K\sqrt{x_{ph}^2 + y_{ph}^2 + L_{tp}^2}}{n_x x_{ph} + n_y y_{ph} + n_z L_{tp}}. \tag{A.4}$$

When the mirror is tilted only in the (x,z) plane, as is the case for the NIF and Omega MMI instruments, then n_x and n_z become simple functions of the tilt angle, ψ, while $n_y = 0$. Then we can write

$$E = \frac{-K\sqrt{x_{ph}^2 + y_{ph}^2 + L_{tp}^2}}{n_x x_{ph} + n_z L_{tp}}. \tag{A.5}$$

This gives the energy on the detector plane, E, as a simple function of the position on the pinhole plane. (Notice that in the above cartoon, n_x and L_{tp} are positive while n_z and x_{ph} are negative. Careful consideration of the geometry will always ensure the above expression produces $E > 0$.)

It is useful to note that frequently (as is the case in the NIF and Omega MMI instruments) allowable values of x_{ph} and y_{ph} may be an order of magnitude smaller than L_{tp}. (For instance, the usable area of the pinhole plane may be several millimeters across, while L_{tp} is typically several centimeters or more.) In that case, $x_{ph}^2 \ll L_{tp}^2$ and $y_{ph}^2 \ll L_{tp}^2$, which gives rise to the following approximation:

$$E \approx \frac{-KL_{tp}}{n_x x_{ph} + n_z L_{tp}}. \tag{A.6}$$

This treatment shows the Bragg energy can be regarded as a strong function of x_{ph} but a weak function of y_{ph}.

Alternatively, we may write

$$\hat{n} \cdot \hat{v} = \sin\varphi \implies \frac{-n_x x_{ph} - n_y y_{ph} - n_z L_{tp}}{\sqrt{x_{ph}^2 + y_{ph}^2 + L_{tp}^2}} = \sin\varphi. \tag{A.7}$$

If we again choose the coordinate system for the flat-mirror system such that $n_y = 0$, then this leads to a quadratic equation in x_{ph}:

$$\left(n_x^2 - \sin^2\varphi\right) x_{ph}^2 + \left(2L_{tp} n_x n_z\right) x_{ph} + \left(n_z^2 L_{tp}^2 - \sin^2\varphi\left[y_{ph}^2 + L_{tp}^2\right]\right) = 0 \tag{A.8}$$

Generally, the maximum allowable value of y_{ph} will be at least an order of magnitude lower than L_{tp}, so $y_{ph}^2 << L_{tp}^2$. In such a case the y-dependence becomes negligible, and the above expression simplifies to

$$\left(n_x^2 - \sin^2\varphi\right) x_{ph}^2 + \left(2L_{tp} n_x n_z\right) x_{ph} + L_{tp}^2\left(n_z^2 - \sin^2\varphi\right) = 0 \tag{A.9}$$

So we again find the Bragg energy has a negligible dependence upon y_{ph}, as long as $L_{tp} > y_{ph}$. In that case, the x-position on the pinhole plane is determined by the Bragg angle, φ, as follows:

$$\begin{aligned} x_{ph} &= \frac{-2L_{tp} n_x n_z \pm \sqrt{4L_{tp}^2 n_x^2 n_z^2 - 4L_{tp}^2\left(n_x^2 - \sin^2\varphi\right)\left(n_z^2 - \sin^2\varphi\right)}}{2\left(n_x^2 - \sin^2\varphi\right)} \\ &= \frac{-L_{tp} n_x n_z \pm L_{tp}\sqrt{n_x^2 n_z^2 - \left(n_x^2 n_z^2 - n_x^2\sin^2\varphi - n_z^2\sin^2\varphi + \sin^4\varphi\right)}}{n_x^2 - \sin^2\varphi}. \end{aligned} \tag{A.10}$$

Because $\hat{n}$ is a unit vector and since we have chosen the coordinate system such that $n_y = 0$, $n_x^2 + n_z^2 = 1$. Thus

$$x_{ph} = L_{tp}\left(\frac{-n_x n_z \pm \sin\varphi\cos\varphi}{n_x^2 - \sin^2\varphi}\right). \tag{A.11}$$

Using the above definition of K, we can write x_{ph} as an explicit function of Bragg energy, E:

$$x_{ph} = L_{tp}\left(\frac{-n_x n_z E^2 \pm K\sqrt{E^2 - K^2}}{n_x^2 E^2 - K^2}\right) \tag{A.12}$$

B Yorick Code for Calculating Fresnel Diffraction

A simple BASIC routine for calculating Fresnel diffraction can be found in Rees *et al.* [37]. The estimates in Section 3.1.3.2 were computed using a Yorick translation of the Rees algorithm, listed here.

```
/*-----------------------------------------------------------------------------*/
/* Script for estimating Fresnel diffraction at the detector plane of an MMI  */
/* instrument.  The output is a plot of intensity versus radial distance from */
/* the center of the diffraction pattern.                                      */
/*                                                                             */
/* Solid  R, G, B: diffracted intensity via Fresnel (phase zone) calculation  */
/* Dashed R, G, B: Airy disk radius (Fraunhofer)                               */
/* Dotted black:   geometrical blur radius: 0.5*D*(1+mag) (ray optics)        */
/*                                                                             */
/* For now, the aperture is assumed to be centered on a line connecting the   */
/* source and the detector plane.  We can add phases to account for off-axis  */
/* pinholes.                                                                   */
/*                                                                             */
/* Calculations are based on the numerical algorithm published in             */
/*        Rees, W. G. Eur J. Phys. 8 (1987) 49-52                              */
/* which is based on                                                           */
/*        Burch, D. S. Am J. Phys. 53 (1985) 255-260                           */
/*                                                                             */
/* The algorithm was translated as directly as possible from BASIC to Yorick. */
/* The test cases (MMI=9,10) compare quite favorably to the plots in Figures  */
/* 4 & 5 of the Rees paper.  Thus we infer the algorithm is coded accurately. */
/*                                                                             */
/* For Franhofer diffraction, the illumination within the first zero of the   */
/* Bessel function (i.e., the Airy disk) represents 97.6% of the radially-    */
/* integrated intensity profile.                                               */
/*                                                                             */
/* Therefore, in the Fresnel case, it is useful to identify the radius        */
/* that encloses 97.6% of the radially-integrated intensity profile.          */
/*                                                                             */
/*                                                  Last rev: IT; 08 Feb 2016 */
/*-----------------------------------------------------------------------------*/

/*------------*/
/* Parameters */
/*------------*/

m2mu = 1.e+6; // 1 meter = 1.e6 microns
mu2m = 1.e-6; // 1 micron = 1.e-6 meters
```

```
m2mm = 1.e+3; // 1 meter = 1.e3 millimeters
mm2m = 1.e-3; // 1 mm = 1.e-3 m
npts = 500;

// MMI defines the instrument setup
//    1 = NIF, 10 micron pinholes
//    2 = NIF, 35 micron pinholes
//    3 = NIF, 50 micron pinholes
//    4 = Omega, 5 micron pinholes
//    5 = Omega, 10 micron pinholes
//    6 = Omega, 15 micron pinholes // This is right on the near/far boundary
                                    // (At 17.25 mu, all energies are Fresnel)
//    7 = Omega, 35 micron pinholes
//    8 = Omega, 50 micron pinholes
//    9 = Test: Burch/Rees, 3 Fresnel zones
//   10 = Test: Burch/Rees, 5 Fresnel zones

for(MMI = 1; MMI <=6; MMI++){
//for(MMI = 9; MMI <=10; MMI++){
/*-----------------------------------*/
/* Loop over MMI settings begins here */
/*-----------------------------------*/

lle_geom = nif_geom = 0;

if(MMI==1){ // NIF MMI, 10 micron pinholes
  nif_geom = 1;
  D = 10.0 * 1.e-6; // [m]
  file = "nif_10mu_rees_fresnel";
  //xmax = 200.0 * mu2m;  // 200 microns
  xmax = 50.0 * mu2m;  // 50 microns
  plot_fraun = 0;
}

if(MMI==2){ // NIF MMI, 35 micron pinholes
  nif_geom = 1;
  D = 35.0 * 1.e-6; // [m]
  file = "nif_35mu_rees_fresnel";
  xmax = 200.0 * mu2m;  // 200 microns
  plot_fraun = 0;
}

if(MMI==3){ // NIF MMI, 50 micron pinholes
  nif_geom = 1;
  D = 50.0 * 1.e-6; // [m]
  file = "nif_50mu_rees_fresnel";
```

```
  xmax = 200.0 * mu2m;  // 200 microns
  plot_fraun = 0;
}

if(MMI==4){ // Omega MMI, 5 micron pinholes
  lle_geom = 1;
  D = 5.0 * 1.e-6; // [m]
  file = "lle_05mu_rees_fresnel";
  //xmax = 150.0 * mu2m;  // 150 microns
  xmax = 50.0 * mu2m;  // 50 microns
  plot_fraun = 0;
}

if(MMI==5){ // Omega MMI, 10 micron pinholes
  lle_geom = 1;
  D = 10.0 * 1.e-6; // [m]
  file = "lle_10mu_rees_fresnel";
  //xmax = 150.0 * mu2m;  // 150 microns
  xmax = 50.0 * mu2m;  // 50 microns
  plot_fraun = 0;
}

if(MMI==6){ // Omega MMI, 15 micron pinholes
  lle_geom = 1;
  D = 15.0 * 1.e-6; // [m]
  file = "lle_15mu_rees_fresnel";
  //xmax = 150.0 * mu2m;  // 150 microns
  xmax = 100.0 * mu2m;  // 100 microns
  plot_fraun = 0;
}

if(MMI==7){ // Omega MMI, 35 micron pinholes
  lle_geom = 1;
  D = 35.0 * 1.e-6; // [m]
  file = "lle_35mu_rees_fresnel";
  xmax = 250.0 * mu2m;  // 250 microns
  plot_fraun = 0;
}

if(MMI==8){ // Omega MMI, 50 micron pinholes; RMS
  lle_geom = 1;
  D = 50.0 * 1.e-6; // [m]
  file = "lle_50mu_rees_fresnel";
  xmax = 250.0 * mu2m;  // 250 microns
  plot_fraun = 0;
}
```

```
if(MMI==9){ // Test case: Burch/Rees with 3 Fresnel zones
  mmi_str = "Burch/Rees: 3 Zones";
  radius = 997.0 * 1.e-6; // [m] pinhole radius was 997 microns
  D = 2.0 * radius;
  nlam = 1;
  lambda = 632.8 * 1.e-9; // [m] laser wavelength is 632.8 nm
  EkeV = 12.40/(lambda*1.e10);
  L0 = 0.5236; // [m] this distance corresponds to 3 Fresnel zones
  mag = (494.0-56.7-4.52)/4.52; // From Burch paper
  file = "burch_rees_3zones";
  xmax = 120.0 * mm2m;  // 120 mm
  plot_fraun = 0;  // coplot Fraunhofer diffraction profile?
}

if(MMI==10){ // Test case: Burch/Rees with 5 Fresnel zones
  mmi_str = "Burch/Rees: 5 Zones";
  radius = 997.0 * 1.e-6; // [m] pinhole radius was 997 microns
  D = 2.0 * radius;
  nlam = 1;
  lambda = 632.8 * 1.e-9; // [m] laser wavelength is 632.8 nm
  EkeV = 12.40/(lambda*1.e10);
  L0 = 0.3142; // [m] this distance corresponds to 5 Fresnel zones
  mag = (494.0-35.9-4.52)/4.52; // From Burch paper
  file = "burch_rees_5zones";
  xmax = 120.0 * mm2m;  // 120 mm
  plot_fraun = 0;
}

if(lle_geom){
  mmi_str = "Omega MMI";
  ph_str = swrite(format="%2.0f",D*m2mu)+" !mm PH";
  nlam = 3;
  EkeV = [4.5, 5.25, 6.0]; // [keV] titanium
  lambda = (12.4 * 1.e-10)/EkeV; // [m] lam = hc/E = 12.4 (keV-Ang.)/E_keV
  Ltd = 30.145 * 1.0e-2; // [m] TCC / detector distance
  Ltp = 3.155 * 1.0e-2;  // [m] TCC / pinhole plane distance
  L0 = Ltd - Ltp;
  mag = L0/Ltp;
}

if(nif_geom){
  mmi_str = "NIF MMI";
  ph_str = swrite(format="%2.0f",D*m2mu)+" !mm PH";
  nlam = 3;
  EkeV = [8.0, 10.2, 13.0]; // [keV] min, Ge He_alpha, max
```

```
  lambda = (12.4 * 1.e-10)/EkeV; // [m] lam = hc/E = 12.4 (keV-Ang.)/E_keV
  Ltd = 116.667 * 1.0e-2; // [m] TCC / detector distance
  Ltp = 16.667 * 1.0e-2;  // [m] TCC / pinhole plane distance
  L0 = Ltd - Ltp;
  mag = L0/Ltp;
}

ph_str = swrite(format="%2.0f",D*m2mu)+" !mm PH";
xscale = (xmax/mag)/npts;

/*----------------------------*/
/* Define F0 (Fresnel number) */
/*----------------------------*/
F0 = (0.5*D)^2 / (lambda*L0); // radius

// Note that F0~1 is actually a transitional region.  A hard distinction at
// F0=1 is a bit artificial; it's worthwhile to investigate nearby values.
// Here we use F0 = 0.75 based on examination of the F0 variations over pinhole
// size and energy for both the Omega and NIF MMI systems.
fresnel = fraunhofer = 0;
if (max(F0)>=0.75) {fresnel = 1;    regime_str = "FRESNEL (near field)";}
if (max(F0)<0.75)  {fraunhofer = 1; regime_str = "FRAUNHOFER (far field)";}

/*--------------------------------------------------------------------*/
/* Define radius of geometrical blur disk at the detector (ray optics) */
/*--------------------------------------------------------------------*/
R_geom = 0.5 * D * (1 + mag);
R_geom *= m2mu;

/*-------------------------------------------------*/
/* For comparison, the Fraunhofer diffraction radius */
/* (i.e. the first zero of the Airy disk).          */
/*-------------------------------------------------*/
R_Airy = 1.22 * lambda * L0 / D; // All values are in [m] here
R_Airy *= m2mu; // This is DEFINED at the detector, so no mag factor [mu]

/*--------------------------------------------------------------------------*/
/* Calculate intensity variation as a function of x, via the Rees algorithm */
/*   r0 is the pinhole radius (D/2)                                         */
/*   z  is the axial distance from the PH center to the detector plane (L0) */
/*   x  is the lateral distance on the PH plane, measured from the axis     */
/*--------------------------------------------------------------------------*/
r0 = 0.5 * D;
z = L0;
I = array(0.00, nlam, npts);      // Fresnel intensity pattern
Ifraun = array(0.00, nlam, npts); // Fraunhofer intensity pattern (analytic)
```

```
x1mag = array(0.00, nlam);
x2mag = array(0.00, nlam);
platrms = array(0.00, nlam);
R_97    = array(0.00, nlam);

for(ie=1;ie<=nlam;ie++){ // Loop over wavelengths

  xpt = array(0.00, npts);
  ypt = array(0.00, npts);

  lam = lambda(ie);

  for(ipt=1;ipt<=npts;ipt++){ // Loop over x position (points)

    x = ipt * xscale;
    xpt(ipt) = x; // units on this are meters, as with D, z, lambda, r0, etc.

    azon = pi*lam*z;
    aap  = pi*r0^2;

    // floor function returns "double" rather than "long";
    // doubles are not allowed as array indices
    nmin = long(floor( (r0-x)^2 / (lam*z) ));
    nmax = long(floor( (r0+x)^2 / (lam*z) ));

    zarea = array(0.00,nmax+1);

    if( (x<=r0) & (nmin!=0) ){ // line 100
      for(i=1;i<=nmin;i++){zarea(i) = azon*i;}
    }

    if(nmin!=nmax){ // line 140
      for(i=nmin+1;i<=nmax;i++){
rz = sqrt(i*z*lam);
phi_arg = (r0^2-rz^2-x^2)/(2*x*rz);
psi_arg = (r0^2-rz^2+x^2)/(2*x*r0);
// Float errors in the above can lead to arg > 1 or arg < -1
phi_arg = max(-1.0, phi_arg); phi_arg = min(1.0, phi_arg);
psi_arg = max(-1.0, psi_arg); psi_arg = min(1.0, psi_arg);
phi = acos(phi_arg);
psi = acos(psi_arg);
zarea(i) = rz^2*(pi-phi+0.5*sin(2*phi)) + r0^2*(psi-0.5*sin(2*psi));
      }
    }

    // line 210
```

```
    zarea(nmax+1) = aap;
    for(i=nmax;i>=1;i--){
      zarea(i+1) = zarea(i+1) - zarea(i);
    }

    intensity = 0;
    flag = 1;

    for(i=1;i<=nmax+1;i++){
      intensity += zarea(i)*flag/azon;
      flag *= -1;
    }

    intensity *= intensity;
    ypt(ipt) = intensity;

  } // end of loop over x (radial) position, ipt

  I(ie,:) = ypt(:);

  // Compute the Fraunhofer diffraction pattern for comparison
  // R_Airy should land at the first 0
  //        I = I_0 * (2*J_1(s)/s)^2
  // where J_1 is the Bessel function of the first kind of order 1 and
  // s = k*a*sin(theta) where k=2pi/lambda, a=D/2, and theta = observation angle
  //            s = (pi * D / lambda) * (x/sqrt(L0^2 + x^2))
  // Note that x here is measured ON THE DETECTOR PLANE, thus it is mag*xpt
  s = (pi * D / lam) * mag * xpt/sqrt(L0^2 + (mag*xpt)^2);
  Ifraun(ie,:) = I(ie,1)*(2.0 * bessj1(s)/s)^2;

  // Identify the 97.6% radius for the radially-integrated Fresnel intensity
  dx = mag * m2mu * xpt(dif);
  grow, dx, dx(0);
  IFresnel_total = I(ie,+)*dx(+);  // Radially-integrated intensity to maximum x
  IFresnel_incremental = array(0.0, npts);
  for(idx = 1; idx<=npts; idx++){
    IFresnel_incremental(idx) = sum(I(ie,1:idx)*dx(1:idx));
  }
  Ifraction = IFresnel_incremental / IFresnel_total;
  R_97idx  = max(where(Ifraction < 0.976));
  R_97(ie) = mag * m2mu * xpt(R_97idx);

} // end of loop over wavelengths, ie

// Report R_airy, R_geom, and (if Fresnel) R_97.6%
// R_airy should be appropriate radius when F << 1
```

```
// R_geom appears to be a good approximation in the Fresnel (F ~>1) regime
if(fresnel){
  write,"\t"+mmi_str+"\t"+ph_str+"\t"+regime_str;
  write,"\tE\t\tR_Airy\t\tR_geom\t\tR_97.6%";
  for(ie=1;ie<=nlam;ie++){
    write,EkeV(ie),R_Airy(ie),R_geom,R_97(ie);
  }
}
if(fraunhofer){
  write,"\t"+mmi_str+"\t"+ph_str+"\t"+regime_str;
  write,"\tE\t\tR_Airy\t\tR_geom";
  for(ie=1;ie<=nlam;ie++){
    write,EkeV(ie),R_Airy(ie),R_geom;
  }
}

/*--------------------------------------------------------------------------*/
/* Plot intensity distribution as a function of distance from the axis */
/*--------------------------------------------------------------------------*/
colors = ["red", "green", "blue", "black", "magenta", "cyan", "yellow",
  "red", "green", "blue", "black", "magenta", "cyan", "yellow",
  "red", "green", "blue", "black", "magenta", "cyan", "yellow"];

types = ["solid","solid","solid","solid","solid","solid","solid",
 "dash","dash","dash","dash","dash","dash","dash",
 "dot","dot","dot","dot","dot","dot","dot"];

e_str = swrite(format="%4.2f",EkeV)+" keV";
F0_str = "F = "+swrite(format="%5.3f", F0);
ptitle = mmi_str+": "+ph_str;
leg_str = colors(1:nlam)+": "+e_str+" "+F0_str;
leg_str2 = e_str+": "+F0_str;
leg_str3 = colors(1:nlam)+" dashdot: Fraunhofer";

plot_dir = "../Plots/diffraction/";

psfile = plot_dir + file + ".ps";
epsfile = plot_dir + file + ".eps";
pdffile = plot_dir + file + ".pdf";

window, MMI, hcp=psfile;
fma;
for(ie=1;ie<=nlam;ie++){
  if(fraunhofer){myI = Ifraun(ie,:);}
  if(fresnel){myI = I(ie,:);}
  // Plot radial intensity profile
```

```
  plg, myI(:), mag*xpt*m2mu, marks=0, width=2.0, color=colors(ie), legend=leg_str(ie);
  // Mark Airy disk radii
  plg, [0.0, max(I)], [R_Airy(ie),R_Airy(ie)], marks=0, width=2.0, color=colors(ie), type="dash", le
  // Mark geometrical shadow radius (blur disk)
  plg, [0.0, max(I)], [R_geom, R_geom], marks=0, width=2.0, color="black", type="dot", legend = " ";
  // Mark the 97.6% radius, for the Fresnel cases
  if(fresnel){
    plg, [0.0, 0.66*max(I)], [R_97(ie),R_97(ie)], marks=0, width=2.0,
      color=colors(ie), type="dashdot", legend=" ";
  }
  // Write F value for each energy
  plt, leg_str2(ie), 0.5*mag*xpt(0)*m2mu, max(I)*(0.95-0.07*ie),tosys=1;

}
xytitles,"x_detector_ [!mm]", "Diffracted Intensity", [-0.005, 0.00];
pltitle,ptitle;
limits;
hcp;
hcp_finish;
eps,epsfile;
pdf,pdffile;

/*--------------------------------*/
/* End of loop over MMI settings. */
/*--------------------------------*/
}
```

References

[1] Yaakobi, Barukh, Marshall, Fredric J., and Bradley, David K. "Pinhole-array x-ray spectrometer for laser-fusion experiments," Appl. Opt. **37** (34), 8074 (1998).

[2] Koch, J. A., Barbee, T. W., Izumi, N., et al. "Multispectral x-ray imaging with a pinhole array and a flat Bragg mirror," Rev. Sci. Instrum. **76**, 073708 (2005). (*Note:* Equation 11 of this reference contains a typographical error, as noted in Section 2.2.)

[3] Izumi, N., Barbee, T. W., Koch, J. A., et al. "Reconstruction of quasimonochromatic images for multispectral x-ray imaging with a pinhole array and a flat Bragg mirror," Rev. Sci. Instrum. **77**, 083504 (2006).

[4] Welser-Sherrill, L., Mancini, R. C., Koch, J. A., et al. "Spectroscopic determination of temperature and density spatial profiles and mix in indirect-drive implosion cores," Phys. Rev. E. **76**, 056403 (2007).

[5] Hsu, S. C., Joshi, T. R., Hakel, P., Vold, E. L., Schmitt, M. J., Hoffman, N. M., Rauenzahn, R. M., Kagan, G., Tang, X.-Z., Mancini, R. C., Kim, Y., Herrmann, H. W. "Observation of Interspecies Ion Separation in Inertial-Confinement-Fusion Implosions via Imaging X-Ray Spectroscopy," LA-UR-16-23658 (submitted).

[6] Kyrala, G. A., Martinson, Drew D, Polk, Paul J. Jr. "Implementation of a New Multiple Monochromatic X-ray 2D imager at NIF," LA-UR-13-26310.

[7] Rybicki, George B., and Lightman, Alan P. Radiative Processes in Astrophysics. John Wiley & Sons, New York (1979).

[8] D. H. Munro, "Yorick: An Interpreted Language", distributed with the Yorick source code. (© 2005, The Regents of the University of California, produced at the Lawrence Livermore National Laboratory: UCRL-CODE-155996.)

[9] Baumgaertel, J. A., Bradley, P. A., Hsu, S. C., Cobble, J. A., Hakel, P., Tregillis, I. L., Krasheninnikova, N. S., Murphy, T. J., Schmitt, M. J., Shah, R. C., Obrey, K. D., Batha, S., Johns, H., Joshi, T., Mayes, D., Mancini, R. C., Nagayama,

T. "Observation of early shell-dopant mix in OMEGA direct-drive implosions and comparisons with radiation-hydrodynamic simulations," Phys. Plasmas **21**, 052706 (2014).

[10] Hakel, P., Kyrala, G. A., Bradley, P. A., Krasheninnikova, N. S., Murphy, T. J., Schmitt, M. J., Tregillis, I. L., Kanzleieter, R. J., Batha, S. H., Fontes, C. J., Sherrill, M. E., Kilcrease, D. P., Regan, S. P. "X-ray spectroscopic diagnostics and modeling of polar-drive implosion experiments on the National Ignition Facility," Phys. Plasmas **21**, 063306 (2014).

[11] Hakel, Peter. "FESTR: Finite-Element Spectral Transfer of Radiation spectroscopic modeling and analysis code," Computer Physics Communications, in press (2016).

[12] Regan, Sean. "Conceptual Design Review for the NIF Hot Spot X-Ray Spectrometer (HSXRS)," presentation slides, 21 July 2009.

[13] Kyrala, George. Analysis of absolutely calibrated Supersnout-II data. Private communication. (Email of 04 Dec 2012: "Spectrum from N121119"; data of 19 Nov 2012).

[14] Regan, Sean. "Supersnout II: first look DIME implosion with Ge-doped CH inner layer N121119," presentation slides, 21 Nov 2012.

[15] Kyrala, George. "Using Supersnout Signals to Calibrate MMI Photometrics," memo draft, 07 January 2013.

[16] Minano, J. C. "Application of the conservation of etendue theorem for 2-D subdomains of the phase space in nonimaging concentrators," Appl. Opt. **23** (12), 2021 (1984).

[17] Hsu, S. C. Private communication. (Email of 13 Sep 2016: "Re: MMI Properties".)

[18] `http://henke.lbl.gov/optical_constants/`

[19] Speriosu, V. S., Vreeland, T. "X-ray rocking curve analysis of superlattices," J. Appl. Phys. **56**, 1591, (1984).

[20] Memo from Bill Bowman (Sales Engineer, Rigaku) to Drew Martinson, 22 August 2011.

[21] Henke, B. L., Knauer, J. P., and Premaratne, K. J. "The characterization of x-ray photocathodes in the 0.1-10-keV photon energy region," Appl. Phys., **52**(3), 1509 (1981).

[22] Rochau, G. A., Bailey, J. E., Chandler, G. A., Nash, T. J., Nielsen, D. S., Dunham, G. S., Garcia, O. F., Joseph, N. R., Keister, J. W., Madlener, M. J., Morgan, D. V., Moy, K. J., Wu, M. "Energy dependent sensitivity of microchannel plate detectors," Rev. Sci. Instrum. **77**, 10E323 (2006).

[23] Mancini, Roberto. Design drawings for Omega DDMMI Pinhole Array V4.0 (06/07/05). Private communication. (Email of 22 Feb 2013: "pinhole array designs").

[24] Gillman, Geoff, and Macleod, Iain. "Reconstruction of X-Ray Sources from Penumbral Images," Computer Graphics and Image Processing, **11**, 227 (1979).

[25] Nugent, K. A., and Luther-Davies, B. "Penumbral Imaging of High Energy X-Rays from Laser-Produced Plasmas," Optics Communications, **49**(6), 393 (1984).

[26] Welser, L. A., Mancini, R. C, Koch, J. A., et al. "Processing of multimonochromatic x-ray images from indirect drive implosions at OMEGA," Rev. Sci. Instrum. **74** (3), 1951 (2003).

[27] Nagayama, Taisuke. "Polychromatic Tomography of High Energy Density Plasmas," Ph.D. dissertation, University of Nevada, Reno (2011).

[28] Koch, J. A., Landen, O. L., Barbee, T. W. Jr., et al. "High-energy x-ray microscopy techniques for laser-fusion plasma research at the National Ignition Facility," App. Opt. **37**(10), 1784 (1998)

[29] Thomas, C., Rehm, G., Martin, I., and Bartolini, R. "X-ray pinhole camera resolution and emittence measurement," Phys. Rev. ST Accel. Beams **13**, 022805 (2010).

[30] Kyrala, George. Private communication. (Email of 30 Nov 2012: "Re: Meeting on MMI SNR".)

[31] Kyrala, George. Private communication. (Email of 10 Dec 2012: "Re: MMI resolution estimates".)

[32] Shah, Rahul. Private communication. (Email of 10 Dec 2012: "Re: MMI resolution estimates".)

[33] Shah, Rahul. Private communication. (Email of 09 Jan 2014: "your document".)

[34] Jackson, J. D. Classical Electrodynamics. John Wiley & Sons, New York (1975), pages 441-442.

[35] Burch, D. S. "Fresnel diffraction by a circular aperture," Am. J. Phys. **53** (3) 255 (1985).

[36] Mielenz, K. D. "Algorithms for Fresnel Diffraction at Rectangular and Circular Apertures," J. Res. Natl. Inst. Stand. Technol. **103** 497 (1998).

[37] Rees, W. G. "Fresnel diffraction by a circular aperture," Eur. J. Phys. **8** 49 (1987).

[38] Speakman, Scott A. "Introduction to High Resolution X-Ray Diffraction of Epitaxial Thin Films," presentation slides, undated. (`http://prism.mit.edu/xray/documents/3%20Introduction%20to%20HRXRD.pdf`)

[39] Jankowski, A. F., and Makowiecki, D. M. "W/B_4C multilayer x-ray mirrors," Opt. Eng. **30** (12), 2003 (1991).

[40] Christensen, F. E., Shou-Hua, Zhu, Hornstrup, A., Schnopper, H. W., Plag, P., and Wood, J. "X-Ray Study of State-of-the-Art Small d-Spacing W/B_4C Multilayers," Journal of X-Ray Science and Technology **3**, 1 (1991).

[41] Seely, J. F., Gutman, G., Wood, J., et al. "Normal-incidence reflectance of W/B_4C multilayer mirrors in the 34-50-Åwavelength region," App. Opt. **32** (19), 3541 (1993).

[42] Yakshin, A. E., Khodos, I. I., Zhelezniak, I. M., and Erko, A. I. "Fabrication, structure and reflectivity of W/C and W/B_4C multilayers for hard X-ray," Opt. Comm. **118**, 133 (1995).

[43] Vainer, Yu. A., Kluenkov, E. B., Pestov, A. E., et al. "Multilayer X-ray Mirrors Based on W/B_4C with Ultrashort (d = 0.7-1.5 nm) Periods," Journal of Surface Investigation. X-ray, Synchrotron and Neutron Techniques **1** (1), 7 (2007).

[44] MacDonald, Michael A., Schäfers, Franz, and Gaupp, Andreas. "A single W/B_4C transmission multilayer for polarization analysis of soft x-rays up to 1 keV," Optics Express **17** (25), 23290 (2009).

[45] Rigaku data, memo to George Kyrala, 20 June 2011.

[46] Rigaku data, report on multilayer characterization for LANL customer ("Project: W/B_4C Double Multilayer Monochromator (DMM) Set; Customer: LANL"), date unknown.

[47] Wysocki, Fred. Private communication. (Email of 22 November 2010, "Omega MMI geometry".)

[48] Kyrala, George. "DMMI Pinhole Design fro [sic] DIME on NIF," presentation slides, 04 October 2011.

[49] Murphy, Tom. Private communication.

[50] Kyrala, George. Private communication. (DIME meeting, 31 July 2013.)

[51] Mancini, Roberto. Private communcation. (Email of 10 Dec 2012: "Re: MMI resolution estimates".)

[52] Murphy, T. J. "Limits on X-Ray Imager Resolution Due to Photon Counting Statistics," LA-UR-98-1504.

[53] Flippo, K. A., Kline, J. L., Doss, F. W., et al. "Development of a Big Area Backlighter for high energy density experiments," Rev. Sci. Instrum. **85**, 093501 (2014).

[54] Murphy, T., Kyrala, G., Shah, R., et al. "Comments on the utility of MMI for the DIME campaign – *An experimental perspective from P-24*," Memo internal to the DIME campaign (2013).